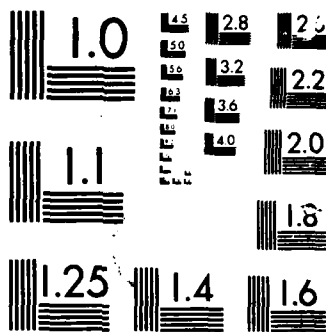


141

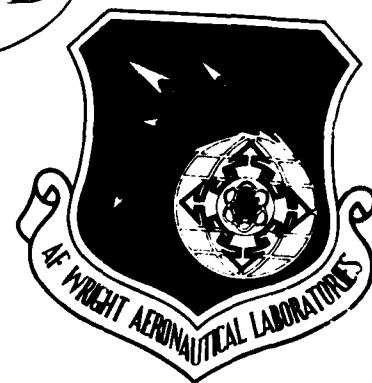
NL

1. 11
 2. 11
 3. 11
 4. 11
 5. 11
 6. 11
 7. 11
 8. 11
 9. 11
 10. 11
 11. 11
 12. 11
 13. 11
 14. 11
 15. 11
 16. 11
 17. 11
 18. 11
 19. 11
 20. 11
 21. 11
 22. 11
 23. 11
 24. 11
 25. 11
 26. 11
 27. 11
 28. 11
 29. 11
 30. 11
 31. 11
 32. 11
 33. 11
 34. 11
 35. 11
 36. 11
 37. 11
 38. 11
 39. 11
 40. 11
 41. 11
 42. 11
 43. 11
 44. 11
 45. 11
 46. 11
 47. 11
 48. 11
 49. 11
 50. 11
 51. 11
 52. 11
 53. 11
 54. 11
 55. 11
 56. 11
 57. 11
 58. 11
 59. 11
 60. 11



AD-A175 679

AFWAL-TR-86-2047



SUPERIONICS

R. F. Wallis
University of California, Irvine
Department of Physics
Irvine, California 92717

October 86

Interim Report for Period April 85 to February 86

Approved for public release; distribution unlimited.

QTHG FILE COPY

AERO PROPULSION LABORTORY

AIR FORCE WRIGHT AERONAUTICAL LABORATORIES

AIR FORCE SYSTEMS COMMAND

WRIGHT-PATTERSON AIR FORCE BASE, OHIO 45433-6563

RECEIVED
JAN 6 1987
A

REPORT DOCUMENTATION PAGE

1a. REPORT SECURITY CLASSIFICATION Unclassified			1d. RESTRICTIVE MARKINGS		
2a. SECURITY CLASSIFICATION AUTHORITY			3. DISTRIBUTION/AVAILABILITY OF REPORT Approval for public release; distribution is unlimited.		
2b. DECLASSIFICATION/DOWNGRADING SCHEDULE			5. MONITORING ORGANIZATION REPORT NUMBER(S) AFWAL-TR-86-2047		
4. PERFORMING ORGANIZATION REPORT NUMBER(S)			7a. NAME OF MONITORING ORGANIZATION Air Force Wright Aeronautical Laboratories Aero Propulsion Laboratory (AFWAL/POOS-2)		
6a. NAME OF PERFORMING ORGANIZATION University of California, Irvine		6b. OFFICE SYMBOL (If applicable)	7b. ADDRESS (City, State and ZIP Code) WPAFB, OH 45433-6563		
6c. ADDRESS (City, State and ZIP Code) Irvine, California 92717		8a. NAME OF FUNDING/SPONSORING ORGANIZATION Defense Advanced Research Projects Agency			
8b. OFFICE SYMBOL (If applicable) DSO		9. PROCUREMENT INSTRUMENT IDENTIFICATION NUMBER F33615-85-C-2501			
8c. ADDRESS (City, State and ZIP Code) Arlington, VA 22209		10. SOURCE OF FUNDING NOS.			
		PROGRAM ELEMENT NO. 62712E 62702E	PROJECT NO. 3145	TASK NO. 22	WORK UNIT NO. 07
11. TITLE (Include Security Classification) Superionics					
12. PERSONAL AUTHOR(S) R. F. Wallis					
13a. TYPE OF REPORT Interim		13b. TIME COVERED FROM 1 Apr 85 to 28 Feb 86		14. DATE OF REPORT (Yr., Mo., Day) 1986 October	
15. PAGE COUNT 49					
16. SUPPLEMENTARY NOTATION					
17. COSATI CODES			18. SUBJECT TERMS (Continue on reverse if necessary and identify by block number)		
FIELD	GROUP	SUB. GR.	Solid-State Battery		
20	12		Fast Ion Conductor		
			Intercalation		
19. ABSTRACT (Continue on reverse if necessary and identify by block number) The ionic conductivity at 100°C of lithium borate glasses doped with lithium sulfate is found experimentally to decrease by three orders of magnitude when the annealing temperature is increased from 515°C to above the crystallization temperature of 532°C. This behavior is correlated with structural changes investigated by Raman spectroscopy. Under suitable conditions, lithium metal can be intercalated into the layered compound InSe. Experimental data for the resistivity as a function of time of intercalation is presented. A simple model is developed to explain the transfer of electrons from the lithium atoms to the InSe layers and is used to quantitatively relate the fraction of electrons transferred to the potential well depth of the InSe. Experimental photoluminescence data for lithium intercalated InSe are presented and interpreted in terms of excitons bound to the Li atoms.					
20. DISTRIBUTION/AVAILABILITY OF ABSTRACT UNCLASSIFIED/UNLIMITED <input checked="" type="checkbox"/> SAME AS RPT. <input type="checkbox"/> DTIC USERS <input type="checkbox"/>			21. ABSTRACT SECURITY CLASSIFICATION Unclassified		
22a. NAME OF RESPONSIBLE INDIVIDUAL Stephen P. Vukson		22b. TELEPHONE NUMBER (Include Area Code) 513-255-5461		22c. OFFICE SYMBOL AFWAL/POOS-2	

TABLE OF CONTENTS

<u>SECTION</u>	<u>PAGE</u>
I. Fast Ion Conduction in $B_2O_3-0.5 Li_2O-xM_2SO_4$ (M-Li or K)	1
1. Effect of Structural Changes on Fast Ion Conduction	1
1.1. Ionic Conductivity of $B_2O_3-0.5Li_2O-0.1$ Li_2SO_4	2
1.2. Raman Scattering of $B_2O_3-0.5Li_2O-0.1$ Li_2SO_4	3
1.3 Effect of Composition on the Stability of Solid Electrolyte $B_2O_3-xLi_2O-yLi_2SO_4$	8
1.4 Glass-Crystalline Transition in Borate Glasses	14
1.4.1. The Breathing Mode $\nu_1(A_1)$ of SO_4^{--}	14
1.4.2. The Breathing Mode of the B_3O_4 Ring	17
1.5. Discussion	20
1.6. Conclusion	24
II. Intercalation in Layered Compounds	25
1. Characteristics of the Intercalation Process	25
2. Intercalation	25
2.1. Time Evolution of Intercalation	29
2.2. Analysis of Saturation of Electrical Conductivity During Intercalation	30
3. Photoluminescence in Layered InSe	38

LIST OF FIGURES

<u>FIGURE</u>		<u>PAGE</u>
1	Temperature Dependence of the $B_2O_3-0.5Li_2O-0.1Li_2SO_4$ Ionic Conductivity for Different Annealing Temperatures.	2
2	Variations of the Ionic Conductivity at $100^{\circ}C$ and of the Activation Energy for Different Annealing Temperatures of the $B_2O_3-0.5Li_2O-0.1Li_2SO_4$.	4
3	Raman Spectra at Room Temperature of $B_2O_3-0.5Li_2O-0.1Li_2SO_4$ for Different Annealing Temperatures.	5
4	Some Structural Units of Crystalline and Amorphous Alkaliborates.	7
5	Raman Spectra at Room Temperature in the Region of the SO_4^{--} Ion Frequencies for Different Annealing Temperatures.	9
6	Comparison of Raman Spectra at Room Temperature for Two Different Glasses, $B_2O_3-0.5Li_2O-0.1Li_2SO_4$ and $B_2O_3-0.5Li_2O-0.1K_2SO_4$, in their Glassy and Crystalline States.	10
7	Raman Spectra of $B_2O_3-0.5Li_2O-yLi_2SO_4$ for $y=0; 0.05; 0.10; 0.15$ at Room Temperature Without Annealing.	11
8	Raman Spectra for $B_2O_3-0.7Li_2O-yLi_2SO_4$ for $y=0.0; 0.42$ at Room Temperature Without Annealing.	12
9	Normal Modes of Vibration of the SO_4^{--} Ion.	13

LIST OF FIGURES (cont.)

<u>FIGURE</u>		<u>PAGE</u>
10	Raman Peaks Corresponding to the Breathing Symmetrical Mode of the B_3O_6 Cycles as a Function of the Li Concentration.	15
11	Structural Group Appearing in the Alkali Borates: Tetraborates and Pentaborates.	16
12	Raman Spectra for Different Annealing Temperatures of $B_2O_3-0.5Li_2O-0.15Li_2SO_4$ Centered at the Mode $\nu_1(A_1)$.	18
13	Raman Spectra of $B_2O_3-0.7Li_2O-0.42Li_2SO_4$ for Different Annealing Temperatures Focussed at the $\nu_1(A_1)$ Vibration of SO_4^{--} .	19
14	Raman Spectra of $B_2O_3-0.5Li_2O-0.1Li_2SO_4$ for Different Annealing Temperatures.	21
15	Raman Spectra of $B_2O_3-0.5Li_2O-0.15Li_2SO_4$ for Different Annealing Temperatures Focussed at the Frequency Region of the Characteristic Modes for Crystalline diborate.	22
16	Raman Spectra of $B_2O_3-0.7Li_2O-0.42Li_2SO_4$ for Different Annealing Temperatures.	23
17	Positions of Li^+ Ions (Solid Circles) in the Van der Waals Gap.	26
18	Energy Level Diagram for Intercalated Lithium under Saturated Conditions.	28
19	Resistivity Versus Time Curve During Li-InSe Intercalation at Room Temperature.	29

LIST OF FIGURES (cont.)

<u>FIGURE</u>		<u>PAGE</u>
20	Conductivity Versus Time Curve During Li-InSe Intercalation at Room Temperature.	30
21	Charge Transfer at Saturation Versus Potential Well Depth for Li-InSe Intercalation.	37
22	Photoluminescence Spectra of the InSe Before (a) and After Lithium Intercalation (b) at 5 K Under 1.916 eV Excitation of a Kr^+ Laser.	39
23	Photoluminescence Spectra of InSe Before (a) and After Lithium Intercalation (b) at 100 K Under 1.916 eV Excitation of a Kr^+ Laser.	40

I. Fast Ion Conduction in $B_2O_3-0.5Li_2O-xM_2SO_4$ ($M=Li$ or K)

1. Effect of Structural Changes on Fast Ion Conduction

Fast ion conduction has been investigated in the borate glasses $B_2O_3-0.5Li_2O-xM_2SO_4$ ($M=Li$ or K) at the Laboratoire de Physique des Solides de l'Université Pierre et Marie Curie, Paris, by M. Balkanski and coworkers. The intent of this work was to investigate the effect of structural changes on the ionic conductivity of the glass. For this purpose temperature annealing has been performed at different temperatures, and the conductivity and structural changes have been studied in each of the annealed samples. The samples were cut from the bulk into parallelepipeds of $3 \times 3 \times 1$ mm³. For inducing the structural change, they were annealed at the annealing temperature (T_A) for one hour and then quenched; all the samples annealed below 513°C were colorless and completely transparent. On the contrary, those annealed at temperatures above 513°C became white and opaque. Two kinds of experiments were performed on polished surfaces with evaporated gold electrodes for the conductivity measurements.

1.1. Ionic Conductivity of $B_2O_3-0.5Li_2O-0.1Li_2SO_4$

The ionic conductivity was deduced from complex impedance measurements between 10^{-2} Hz and 10^4 Hz. The vitreous transition temperature (T_G) and the crystallization temperature (T_C) of this glass are respectively 472°C and 532°C.

Figure 1 shows the temperature dependence of the ionic conductivity σ_i for different annealing temperatures. The conductivity increases with temperature according to the

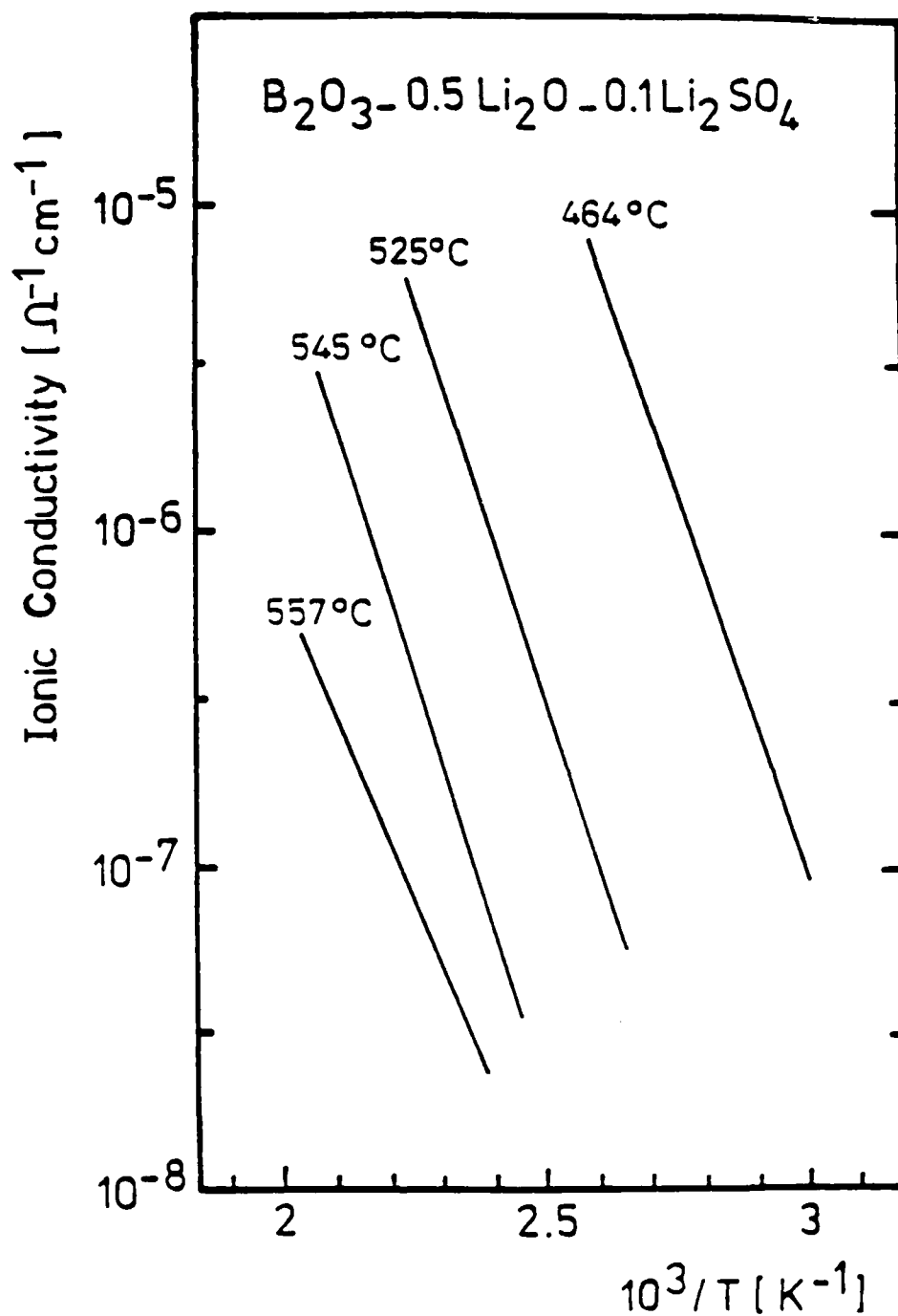


Figure 1: Temperature Dependence of the $B_2O_3-0.5Li_2O-0.1Li_2SO_4$ Ionic Conductivity for Different Annealing Temperatures

exponential law:

$$\sigma_i = \sigma_o \exp (- E_a/kT)$$

where E_a represents the activation energy of the conduction process.

Figure 2 presents simultaneously the variations of the ionic conductivity at 100°C and of the activation energy for different annealing temperatures T_A . For annealing temperatures smaller than 515°C the conductivity increases slightly to reach $7 \times 10^{-6} \Omega^{-1} \text{cm}^{-1}$. These values are in good agreement with those deduced from the experiment at 300°C. For annealing temperatures above 515°C the conductivity decreases rapidly, and the material becomes an insulator with $\sigma_i = 10^{-9} \Omega^{-1} \text{cm}^{-1}$, when the annealing temperature is higher than the crystalline temperature ($T=532^\circ\text{C}$). Between these two points, one would expect that the crystallization is realized in two different stages. At the same time, the activation energy E_a , deduced from the results presented in Figure 1, stays practically constant, ($E_a = 1\text{eV}$), in the glassy state, and then decreases to 0.8 eV after crystallization.

1.2. Raman Scattering of $\text{B}_2\text{O}_3\text{-}0.5\text{Li}_2\text{O-}0.1\text{Li}_2\text{SO}_4$

The Raman spectra of the glass samples were excited by the 514.5nm line of the argon laser. The scattered light was analyzed with the CODERG PH 0 spectrometer with an ITT FW130 photomultiplier connected to a photocounting system.

In Figure 3, the Raman spectra ($\omega > 400 \text{ cm}^{-1}$) of the glass are presented for different annealing temperatures. In the glassy state ($T_A = 475^\circ\text{C}$) the observed spectrum corresponds to an overlapping of the $\text{B}_2\text{O}_3\text{-Li}_2\text{O}$ and SO_4^{--} spectra. The lines due to

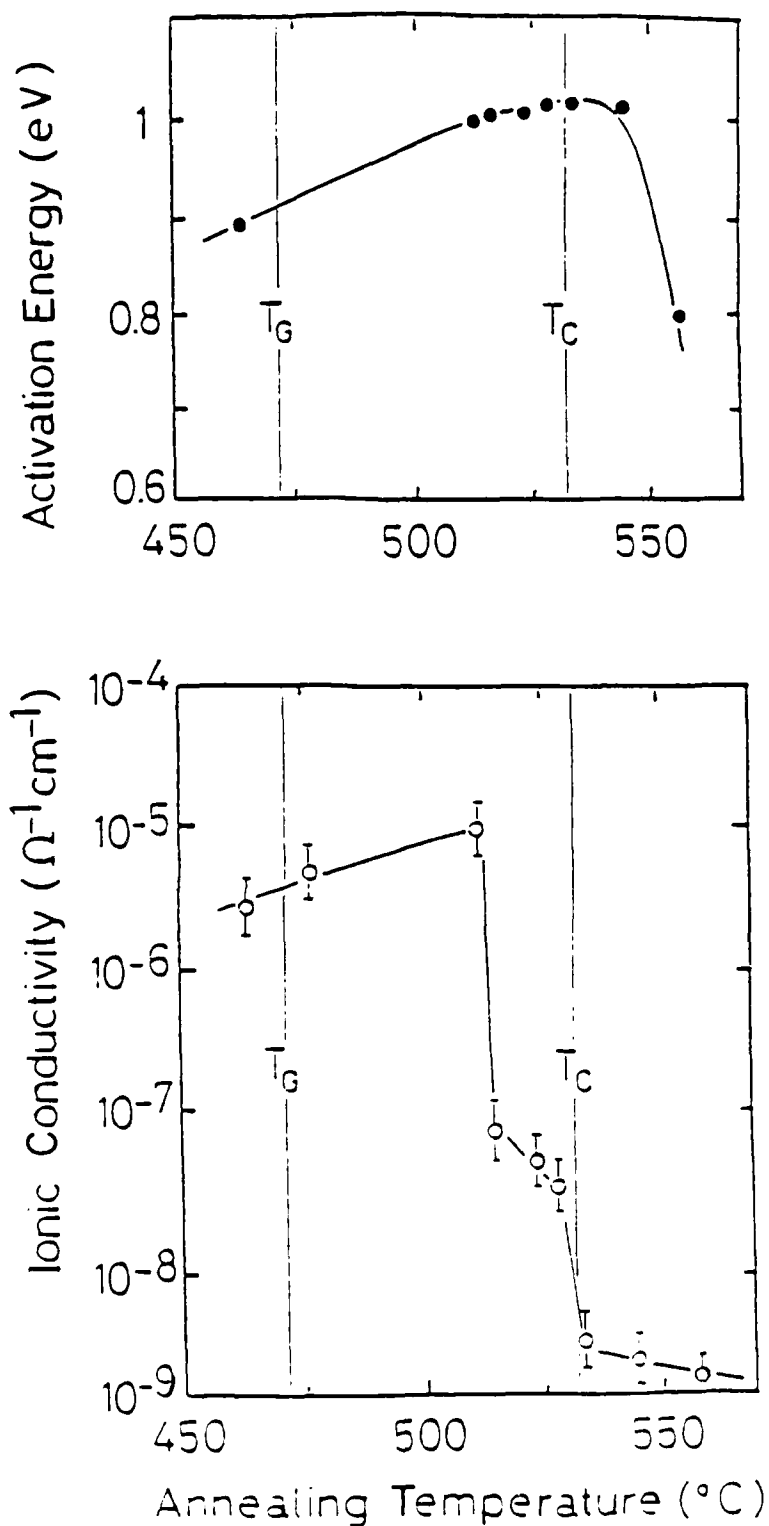


Figure 2: Variations of the Ionic Conductivity at 100°C and of the Activation Energy for Different Annealing Temperatures of $\text{B}_2\text{O}_3\text{-}0.5\text{Li}_2\text{O-}0.1\text{Li}_2\text{SO}_4$

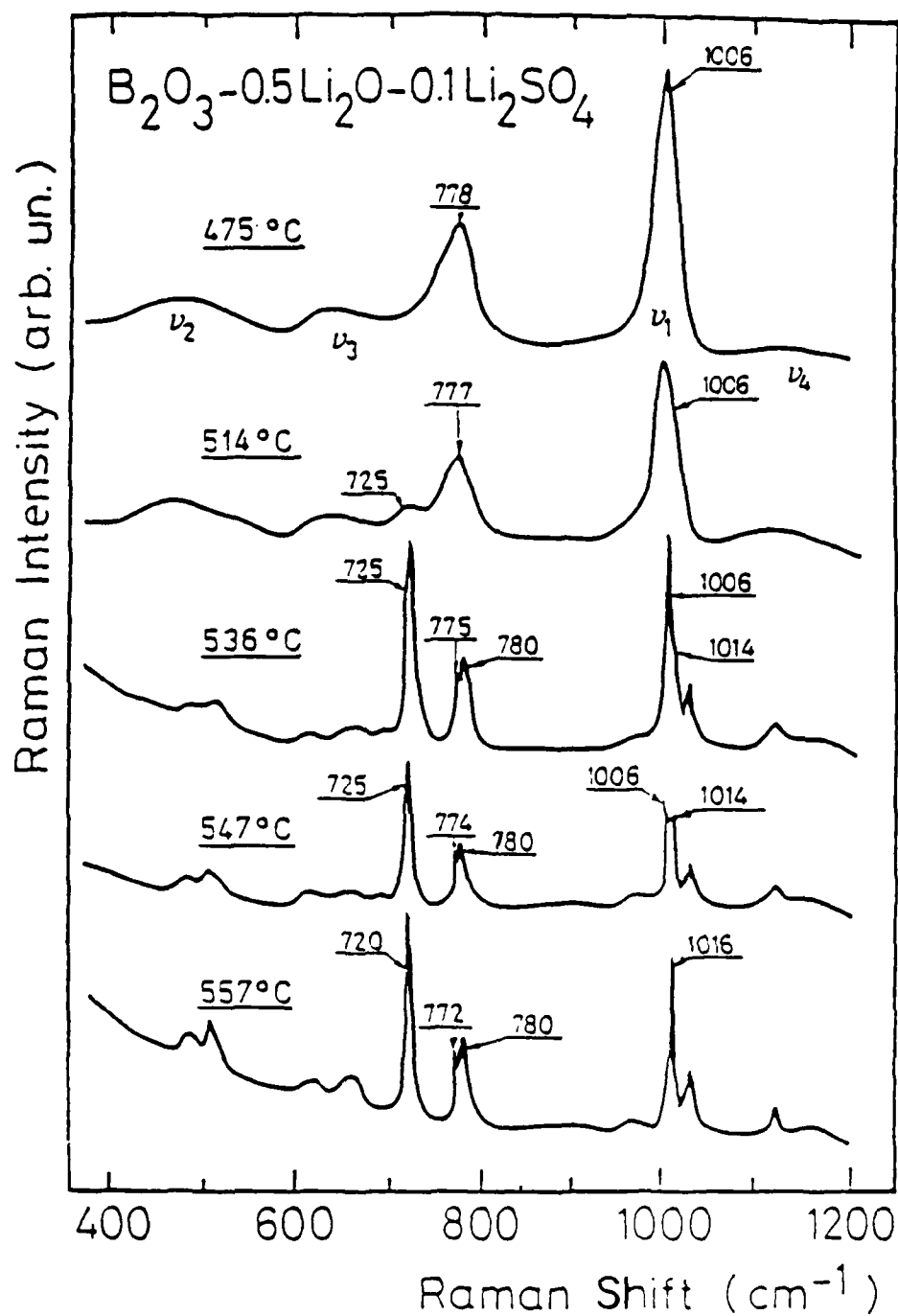


Figure 3: Raman Spectra at Room Temperature of the $B_2O_3-0.5Li_2O-0.1Li_2SO_4$ for Different Annealing Temperatures. Laser wavelength is the 514.5 nm-line.

the tetrahedral sulfate group are clearly seen near 460 cm^{-1} (ν_2), 630 cm^{-1} (ν_3), 1004 cm^{-1} (ν_1) and 1130 cm^{-1} (ν_3) and are analogous to that observed for SO_4^{--} ions in aqueous solutions. This indicates that the sulfate ions are diluted in the vitreous matrix without detectable interaction with the surroundings. The peak observed at 777 cm^{-1} is characteristic of the borate glass matrix and is attributed to the vibration of a six membered borate ring with BO_4 groups. Probably this mode of vibration is also related to triborate groups and to some other groups having more four-fold coordinated boron atoms, such as ditriborate and diborate groups (see Figure 4).

With increase of the annealing temperature two regions of the spectra are deeply modified. They are described below:

The borate glass line region between 700 cm^{-1} and 800 cm^{-1} where a new peak is evident at 725 cm^{-1} and whose intensity increases with the annealing temperature. In the polycrystalline state ($T_A=557^\circ\text{C}$), this spectral region is composed of two lines: 720 cm^{-1} and 790 cm^{-1} . The Raman spectrum of polycrystalline diborate $\text{B}_2\text{O}_3\text{-}0.5\text{Li}_2\text{O}$ shows two lines with the same frequency and the same intensity ratio, which suggests the formation of diborate groups during the crystallization process. The small line at 772 cm^{-1} which appears for annealing temperatures above 530°C indicates the formation of ditriborate groups during the crystallization.

The ν_1 line region of the SO_4^{--} ions where, after annealing at 516°C , a second line, evident at 1016 cm^{-1} appears. As the annealing temperature increases, the intensity

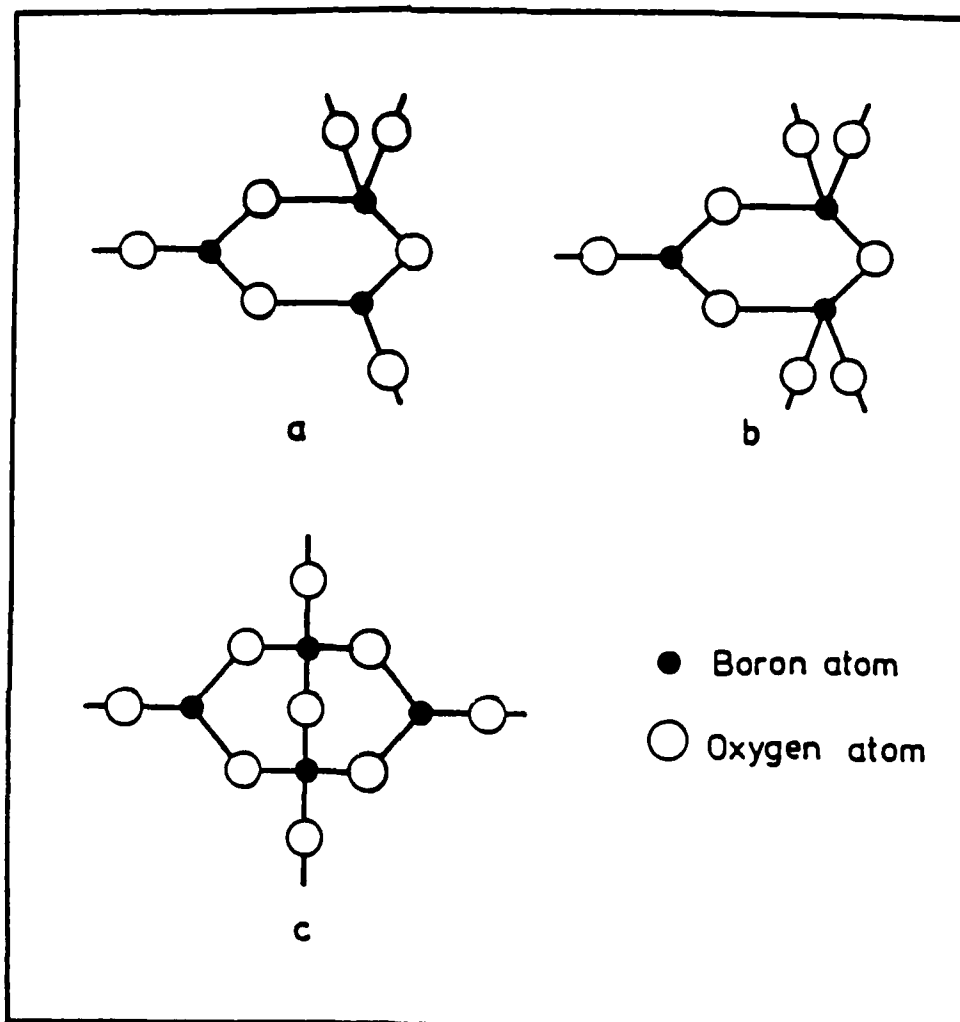


Figure 4: Some Structural Units of Crystalline and Amorphous Alkaliborates:

- a) the triborate group
- b) the ditriborate group
- c) the diborate group.

of this peak increases while that of the previous line at 1006 cm^{-1} decreases and disappears at the crystalline temperature (Figure 5). This new line, attributed to the symmetrical vibration of the tetrahedral SO_4^{--} ion in crystalline lithium sulfate shows that above this temperature the lithium sulfate crystallizes also.

Figure 6 presents the comparison of Raman spectra for two different glasses having the formulas $\text{B}_2\text{O}_3\text{-}0.5\text{Li}_2\text{O-}0.1\text{Li}_2\text{SO}_4$ and $\text{B}_2\text{O}_3\text{-}0.5\text{Li}_2\text{O-}0.1\text{K}_2\text{SO}_4$ in their glassy and crystalline states. In the glassy state, the Raman spectra of the two glasses are similar; those of the polycrystalline material show principally the displacement of the ν_1 line of the SO_4^{--} ion towards lower frequency ($\omega \approx 982\text{ cm}^{-1}$) according to the mass change between lithium and potassium in the sulfate. Here also the measured frequency is in good agreement with the frequency of the symmetrical vibration of the SO_4^{--} ion reported for pure crystalline potassium sulfate ($\omega \approx 984\text{ cm}^{-1}$). This result agrees with the fact that in the glass, the salt seems to be "diluted" in the vitreous matrix without interactions with the surroundings. The sulfate crystallizes after the borate network.

1.3. Effect of Composition on the Stability of the Solid

Electrolyte $\text{B}_2\text{O}_3\text{-}x\text{Li}_2\text{O-}y\text{Li}_2\text{SO}_4$

Investigations on the effects of Li ion concentration are now being developed. The first set of concentrations for $\text{Li}_2\text{O}:x$ and $\text{Li}_2\text{SO}_4:y$ is the following:

$$\begin{array}{ll} x = 0.5 & y = 0.0 \\ " & y = 0.05 \end{array}$$

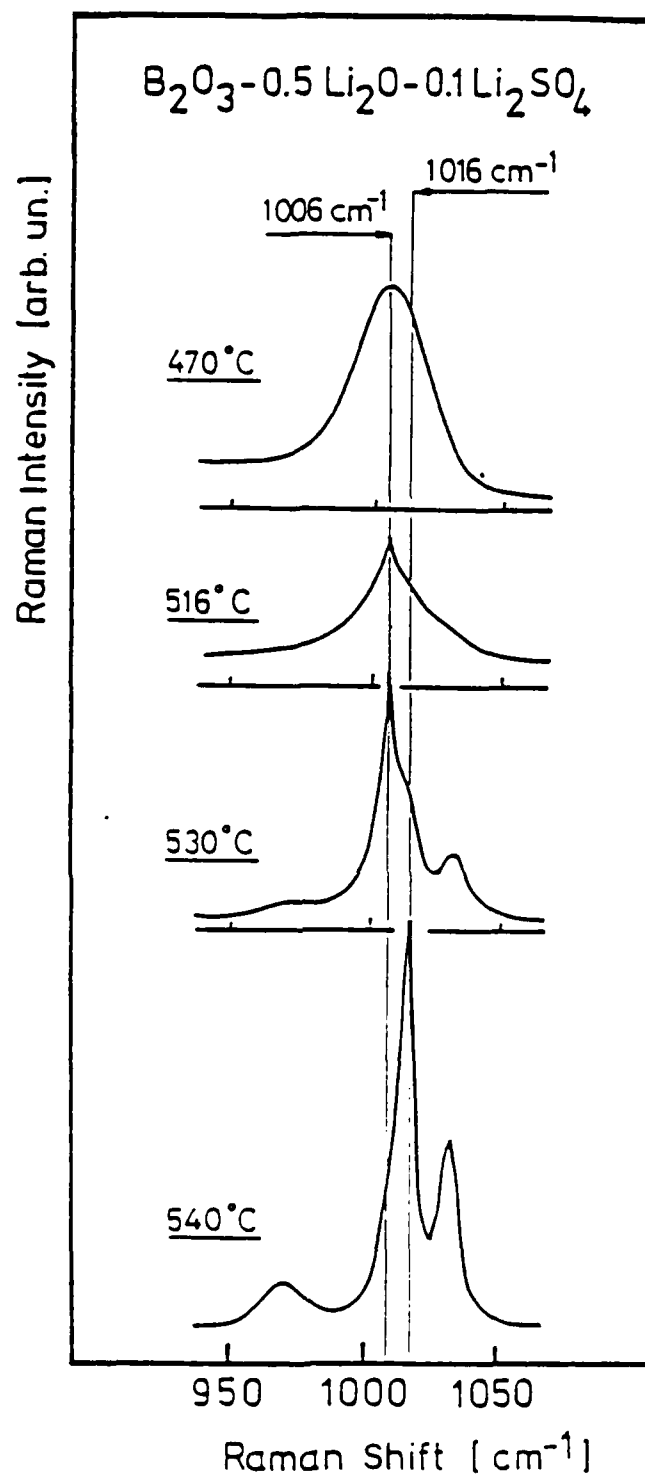


Figure 5: Raman Spectra at Room Temperature in the Region of the SO_4^{2-} Ion Frequencies for Different Annealing Temperatures. Laser wavelength is the 514.5-nm line.

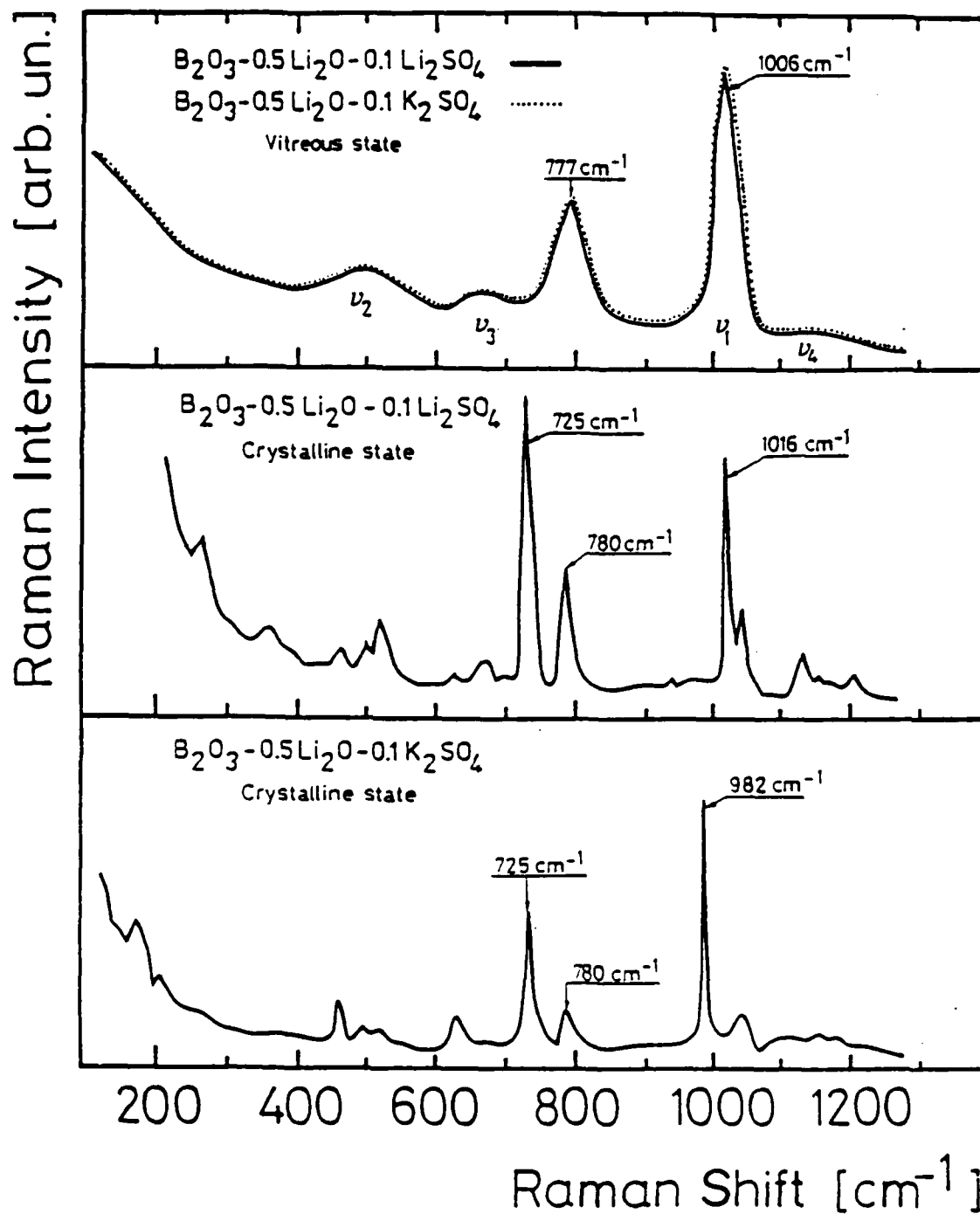


Figure 6: Comparison of Raman Spectra at Room Temperatures for Two Different Glasses, $B_2O_3-0.5Li_2O-0.1Li_2SO_4$ and $B_2O_3-0.5Li_2O-0.1K_2SO_4$, in their Glassy and Crystalline States. Laser wavelength is 514.5-nm line.

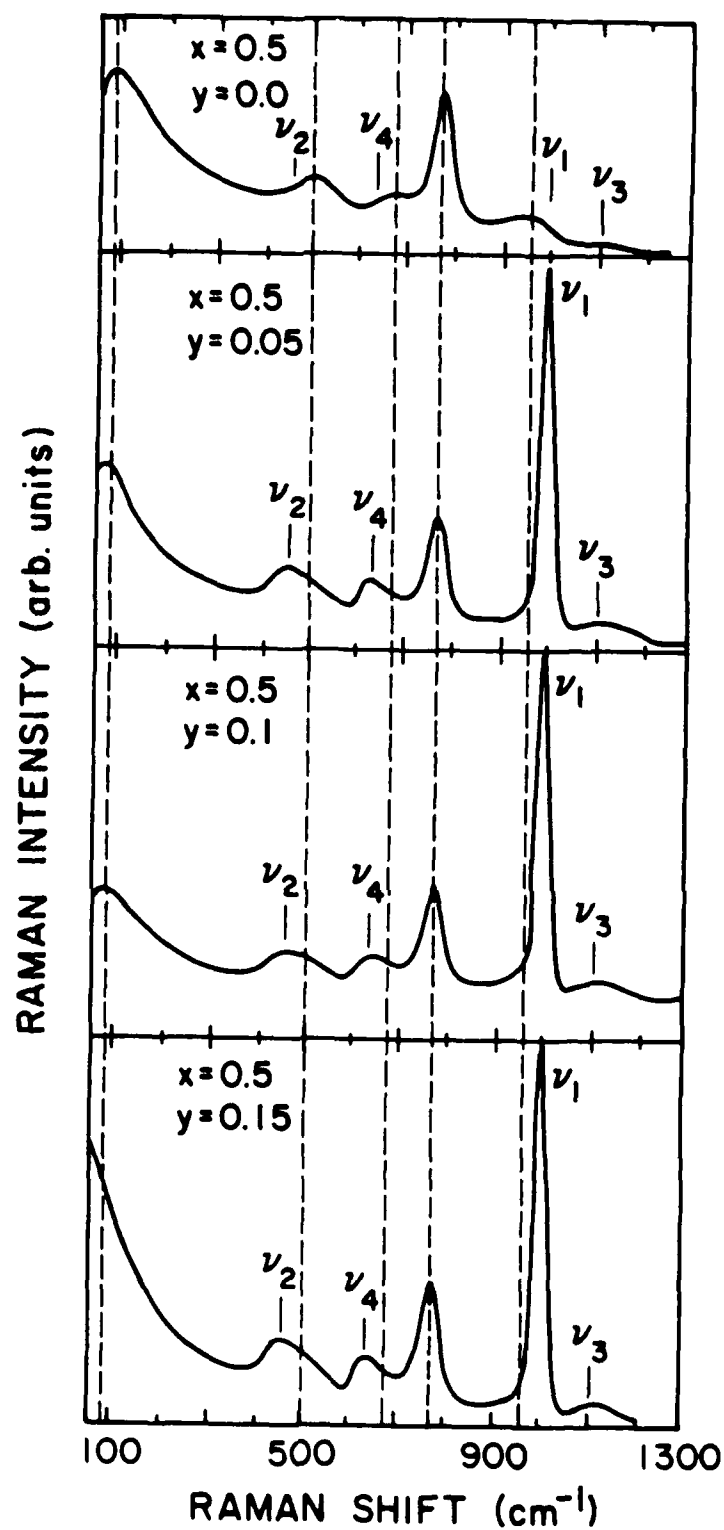


Figure 7: Raman Spectra of $B_2O_3-0.5Li_2O-yLi_2SO_4$ for $y=0$; 0.05; 0.10; 0.15 at Room Temperature Without Annealing.

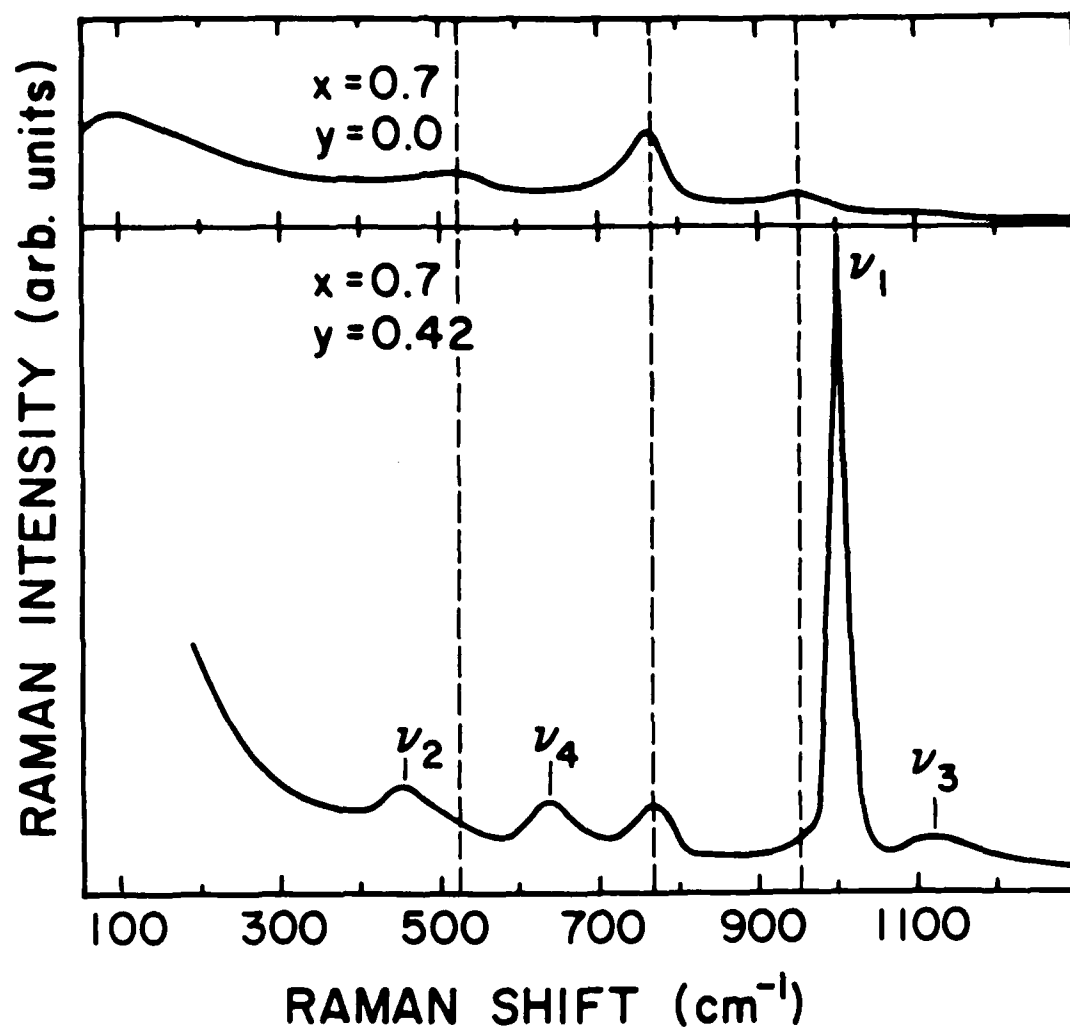


Figure 8: Raman Spectra for $B_2O_3-0.7Li_2O-yLi_2SO_4$ for $y=0.0$; 0.42 at Room Temperature Without Annealing. Laser Beam at 514.5-nm, Resolution 2 cm⁻¹.

$$\begin{array}{ll}
 x = 0.5 & y = 0.10 \\
 " & y = 0.15 \\
 x = 0.7 & y = 0.0 \\
 " & y = 0.42
 \end{array}$$

The Raman spectra of these samples are displayed in Figures 7 and 8.

The spectra shown in these two figures are the superposition of the light scattering spectrum of the borate glass $B_2O_3-xLi_2O$ and the characteristic peaks of the SO_4^{--} anion. The characteristic peaks of SO_4^{--} are situated at 460 cm^{-1} (ν_2), 630 cm^{-1} (ν_4), 1004 cm^{-1} (ν_1), and 1130 cm^{-1} (ν_3) corresponding to the vibrational modes in Figure 9.

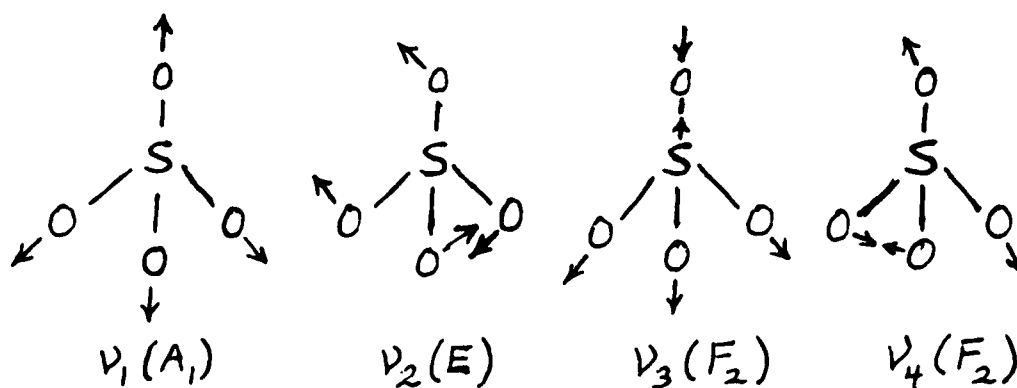


Figure 9. Normal Modes of Vibration of the SO_4^{--} Ion.

The addition of Li_2SO_4 up to the concentrations used in these experiments, $y = 0.42$, does not seem to significantly affect the vibrational frequencies of the borate matrix. The matrix is formed by B_3O_6 rings containing one or more B atoms of coordination number 4: the BO_4 group, for example, whose

characteristic frequency is at 780 cm^{-1} . In the case of borate glasses with $x = 0.5$ the rings are probably mainly triborates but the existence of diborates and ditriborates cannot be excluded. See Figure 4.

Increasing the Li_2O concentration causes the frequency attributed to the BO_4 group breathing mode to decrease, $\omega \approx 770\text{ cm}^{-1}$, and the asymmetry of the band to increase toward the lower energies as shown in Figure 10. This effect seems to be moderated by the addition of Li_2SO_4 .

This change of frequencies and half-width may be due to the appearance in the matrix conformation of more complex configurations in the B_3O_6 rings such as tetraborate and pentaborate groups shown in Figure 11.

1.4. Glass-Crystalline Transition in Borate Glasses

Progressive thermal annealing of borate glasses leads to the crystalline phase of $\text{B}_2\text{O}_3\text{-}x\text{Li}_2\text{O-yLi}_2\text{SO}_4$ through successive configurational transformations of the matrix. The experiments are conducted as follows: the samples are submitted by slow heating to a given annealing temperature T_A and held at that temperature for one hour; then, they are rapidly quenched to room temperature. After this treatment the Raman spectra are taken at room temperature. We will examine successively the different parts of these spectra.

1.4.1. The Breathing Mode $\nu_1(A_1)$ of SO_4^{--}

When the annealing temperature increases progressively from 470°C to 540°C the characteristic peak for the $\text{SO}_4^{--}\nu_1$ mode situated initially at 1006 cm^{-1} first decreases in intensity and

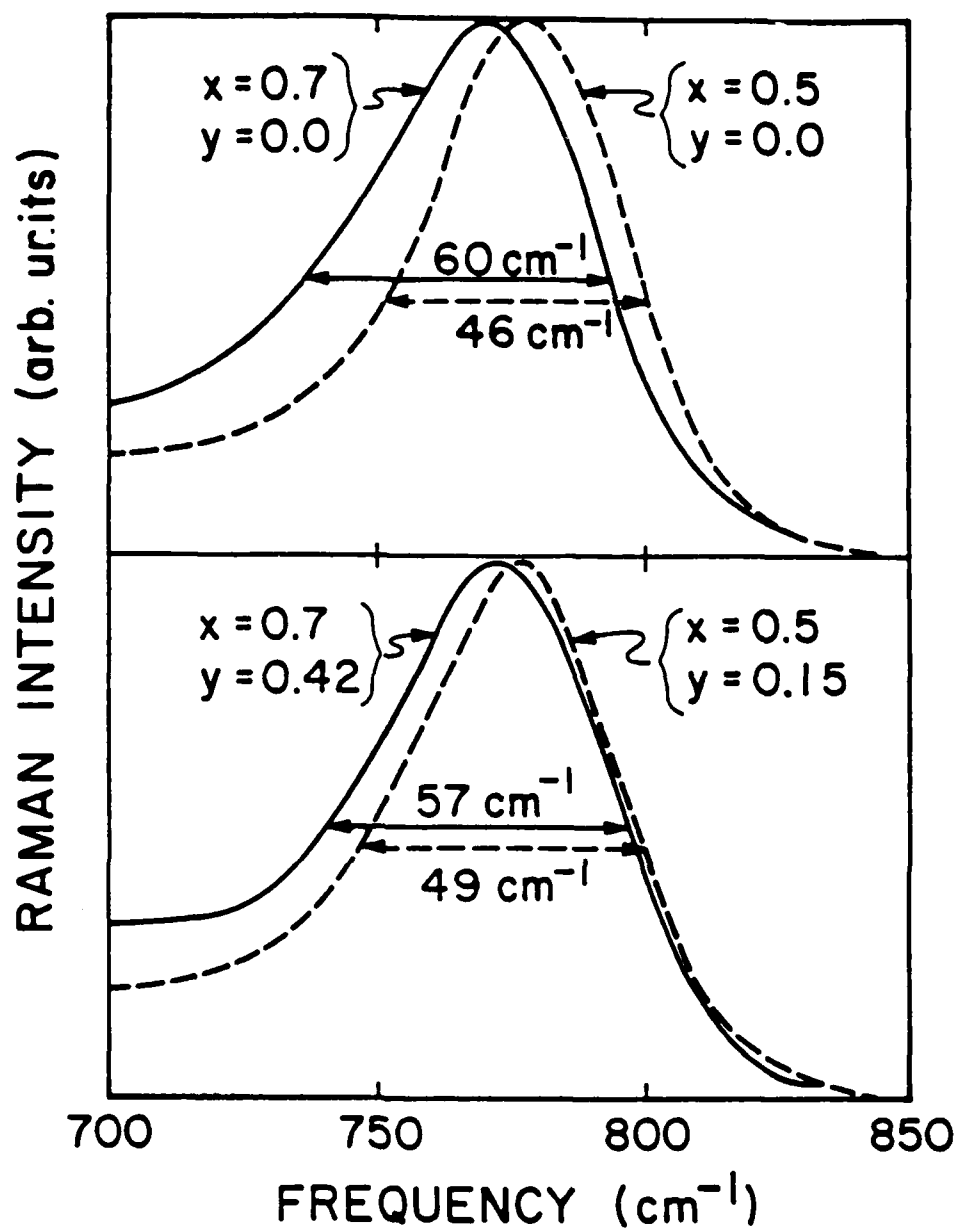
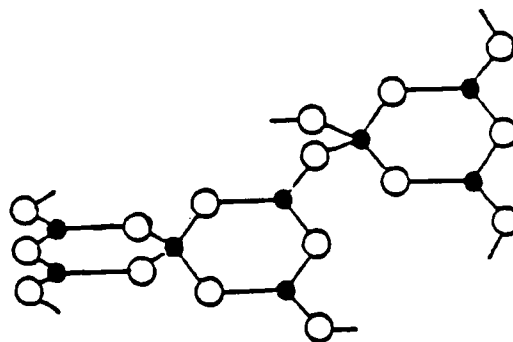


Figure 10: Raman Peaks Corresponding to the Breathing Symmetrical Mode of the B_3O_6 Cycles as a Function of the Li Concentration.

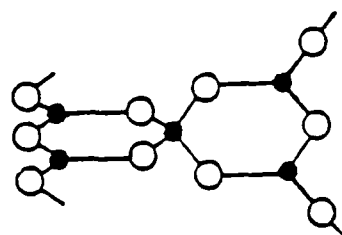
A: $B_2O_3-0.5Li_2O$ and $B_2O_3-0.7Li_2O$

B: $B_2O_3-0.5Li_2O-0.15Li_2SO_4$ and $B_2O_3-0.7Li_2O-0.42Li_2SO_4$.

Spectra taken at room temperature without annealing.



tetraborate group



pentaborate group

Figure 11. Structural Group Appearing in the Alkali Borates:
Tetraborates and Pentaborates.

then disappears. A new peak then appears at 1016 cm^{-1} for annealing temperatures above $T_R = 525^\circ\text{C}$. The peak at 1016 cm^{-1} is still the frequency of the SO_4^{--} breathing mode but now in the crystalline phase of Li_2SO_4 . This transformation can be followed closely in Figures 5, 12, and 13.

The temperature at which the crystallization of Li_2SO_4 occurs, signalled by the appearance of the peak at higher frequencies, depends on the borate composition. For $\text{B}_2\text{O}_3 - 0.5\text{Li}_2\text{O} - 0.1\text{Li}_2\text{SO}_4$ (Figure 5), the new peak at 1016 cm^{-1} shows up at 516°C and is fully developed after the disappearance of the peak at 1006 cm^{-1} at 540°C . For $\text{B}_2\text{O}_3 - 0.5\text{Li}_2\text{O} - 0.15\text{Li}_2\text{SO}_4$ (Figure 12), the peak at 1016 cm^{-1} appears at 525°C and the 1008 cm^{-1} peak disappears completely at 579°C ; whereas for $\text{B}_2\text{O}_3 - 0.7\text{Li}_2\text{O} - 0.42\text{Li}_2\text{SO}_4$ (Figure 13), the second peak is already clearly visible at 475°C and shows a frequency of 1020 cm^{-1} . The first peak initially situated at 1012 cm^{-1} disappears above 511°C . The higher the concentration of Li_2SO_4 , the lower the annealing temperature at which the Li_2SO_4 crystallites appear and the stiffer the $\text{SO}_4^{--} \nu_1$ mode. The stiffening of the breathing mode probably occurs through electrostatic interactions. The higher the ion concentration is, the stronger the repulsive force is among the SO_4^{--} ions. This is an effect equivalent to increasing pressure and therefore stiffening the symmetric mode frequencies.

1.4.2. The Breathing Mode of the B_3O_4 Ring

In the glasses with the diborate matrix $\text{B}_2\text{O}_3 - 0.5\text{Li}_2\text{O} - y\text{Li}_2\text{SO}_4$, above an annealing temperature of 510°C one observes the appearance of a new peak at 725 cm^{-1} , whatever the concentration

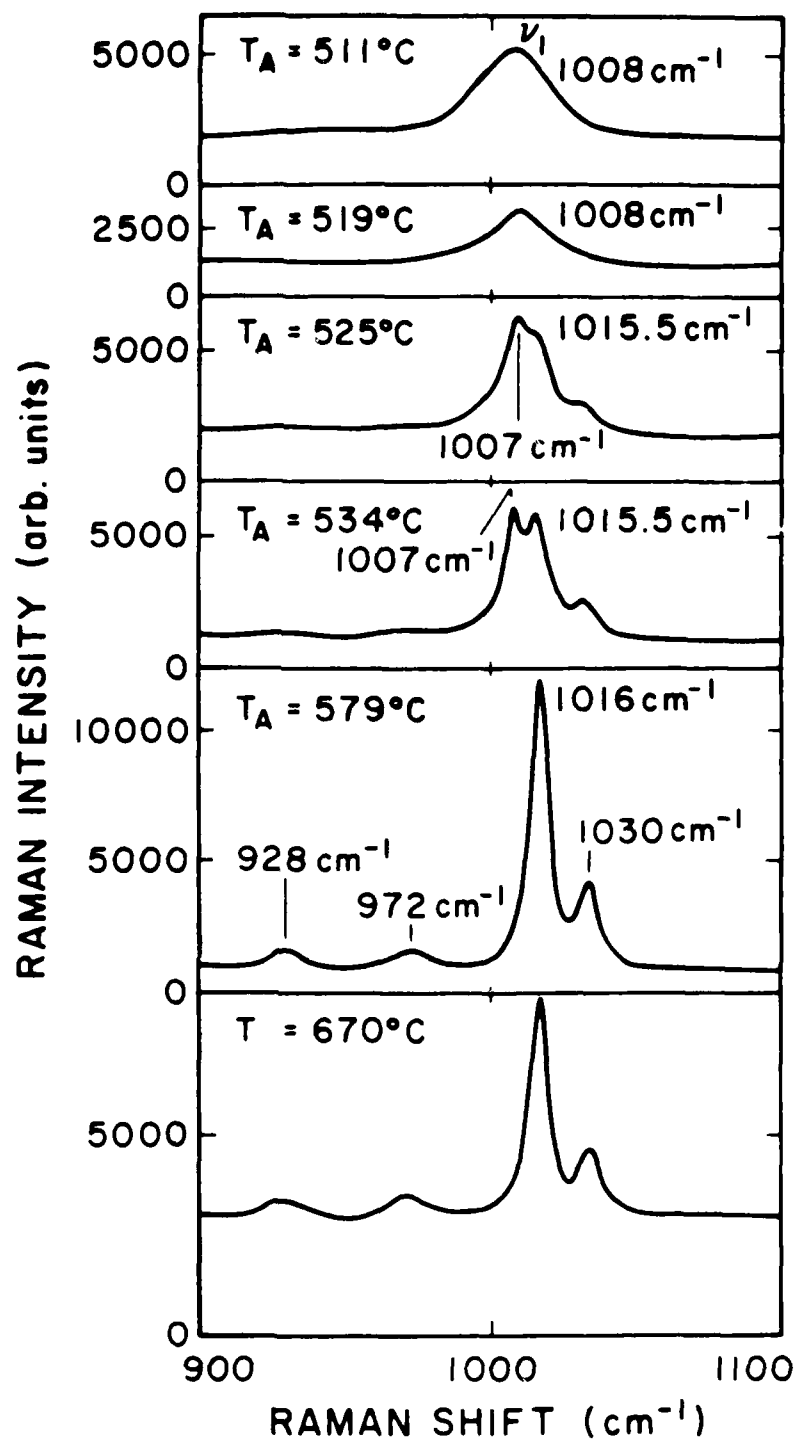


Figure 12: Raman Spectra for Different Annealing Temperatures of $B_2O_3-0.5Li_2O-0.15Li_2SO_4$ Centered at the Mode $\nu_1(A_1)$. Spectra taken at room temperature with a laser beam at 514.5-nm having a power of 250 mW and with an instrumental resolution of 2 cm^{-1} .

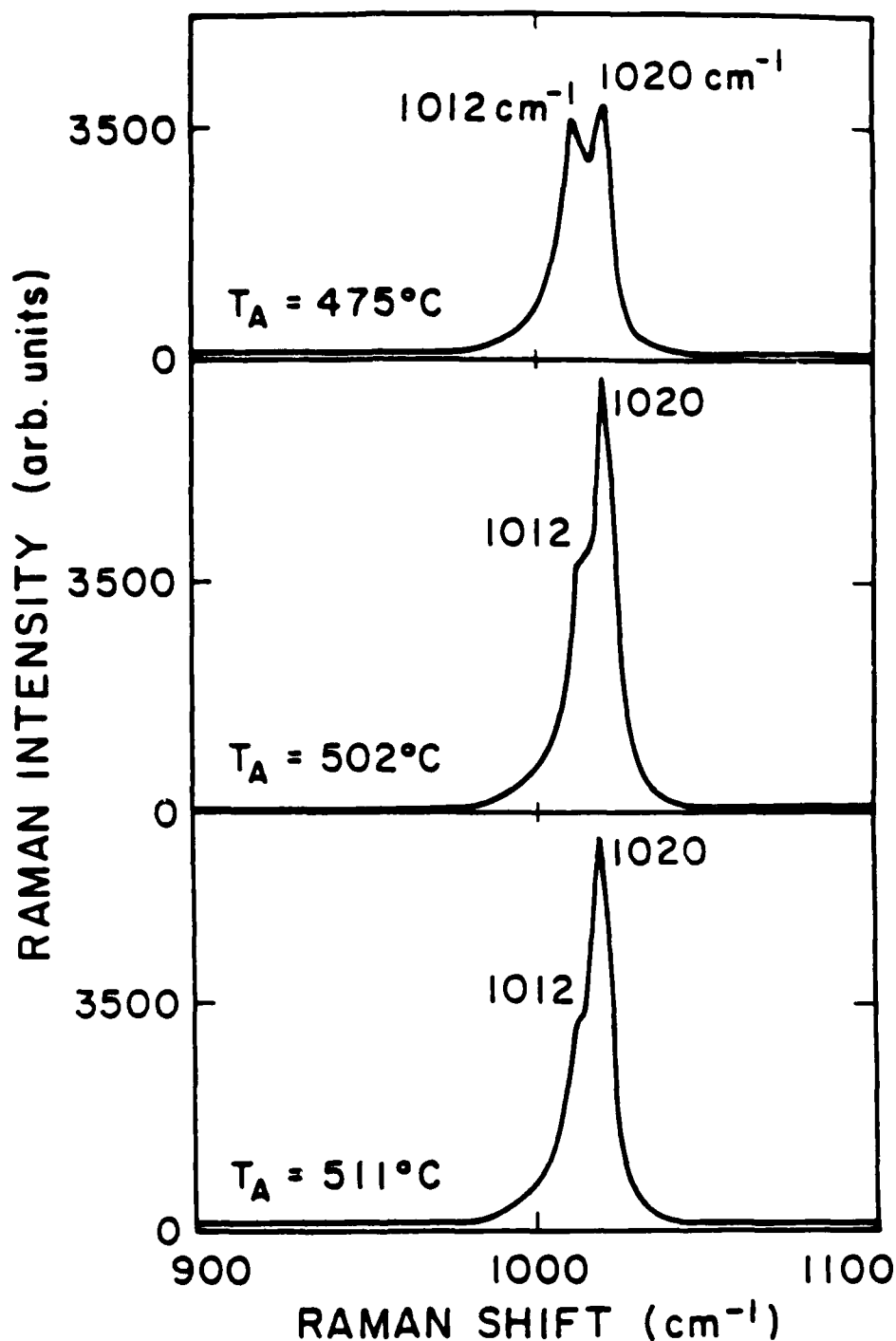


Figure 13: Raman Spectra of $\text{B}_2\text{O}_3\text{-}0.7\text{Li}_2\text{O-}0.42\text{Li}_2\text{SO}_4$ for Different Annealing Temperatures Focussed at the $\nu_1(\text{A}_1)$ Vibration of SO_4^{--} . Spectra are taken at room temperature with a laser beam at 514.5-nm having a power of 250 mW and an instrumental resolution of 2 cm^{-1} .

y might be, as shown in Figures 14 and 15. For annealing temperatures above 560°C the observed spectrum is identical to that of crystalline diborate $B_2O_3 - 0.5Li_2O$. The crystallization of the borate matrix into the forms of diborate is also accompanied by the appearance of a peak at 1030 cm^{-1} (Figures 5, 12, and 14).

Notice also the appearance in the crystalline phase of a weak peak situated at 772-774 cm^{-1} attributed to the formation of ditriborate groups.

In Figure 16 are shown the Raman spectra of $B_2O_3 - 0.7Li_2SO_4 - 0.42Li_2SO_4$. Already at an annealing temperature of 475°C, a set of 3 bands at 620 cm^{-1} , 655.5 and 666.5 cm^{-1} due to the ν_4 SO_4^{--} vibrations appears. This demonstrates that, even at an annealing temperature of 475°C, Li_2SO_4 crystallites are already formed.

1.5 Discussion

The comparison of the experiments described in Sections 1.1, 1.2, and 1.3 is very interesting because it suggests a possible correlation between the structural change and the ionic conductivity variations.

The Raman scattering shows clearly that in the two limiting states of the material, the structure consists of borate rings with different numbers of BO_4^- groups. The BO_4^- groups are singly charged anions with very large ionic radii, the presence of such anions being favorable for ionic conduction. The formation of ditriborate gives an increase in the number of such groups and probably is a reason for the increase of conductivity

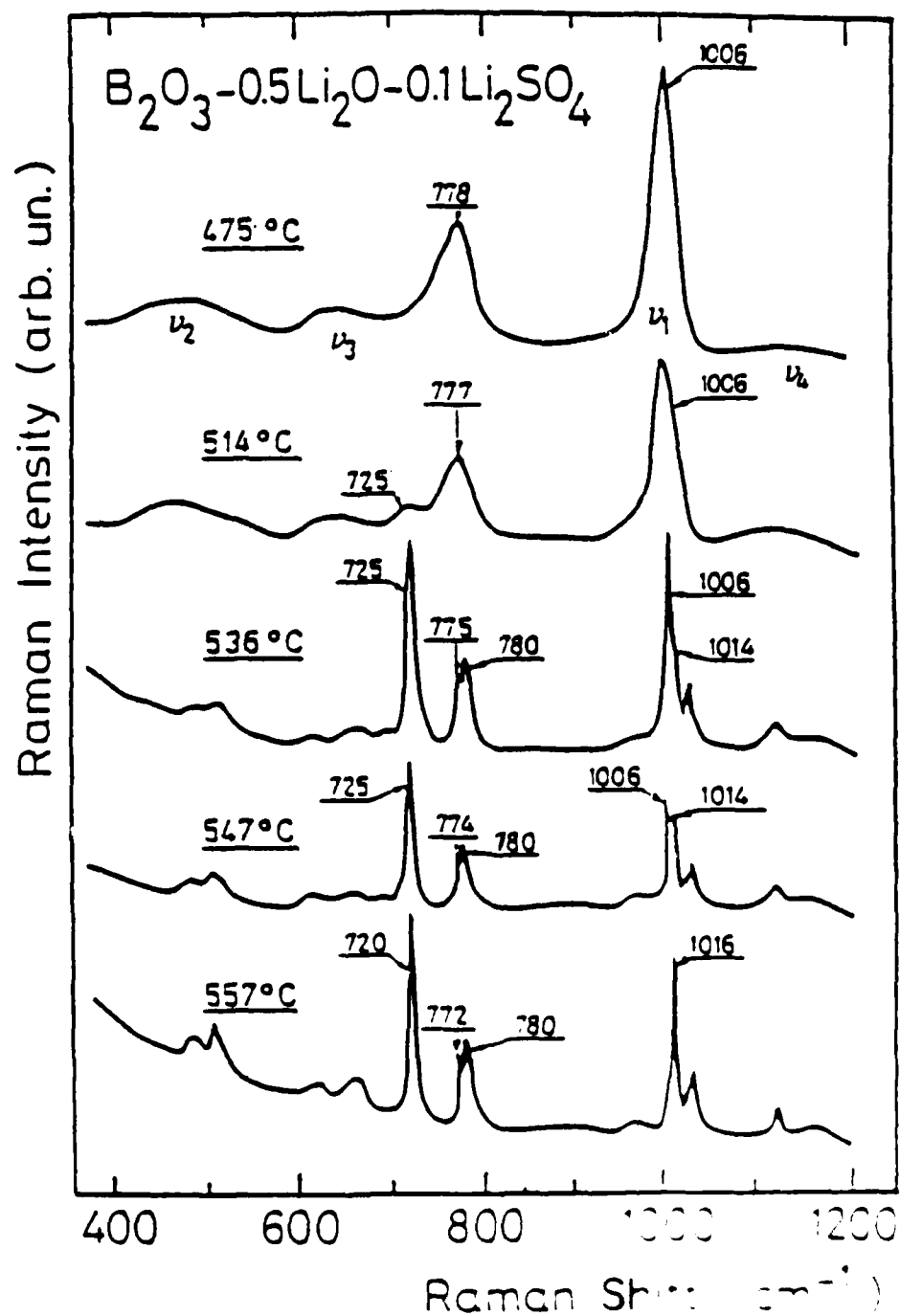


Figure 14: Raman Spectra of $B_2O_3-0.5Li_2O-0.1Li_2SO_4$ for Different Annealing Temperatures. Spectra taken at room temperature with a laser beam at 514.5-nm and a resolution of 2 cm^{-1} .

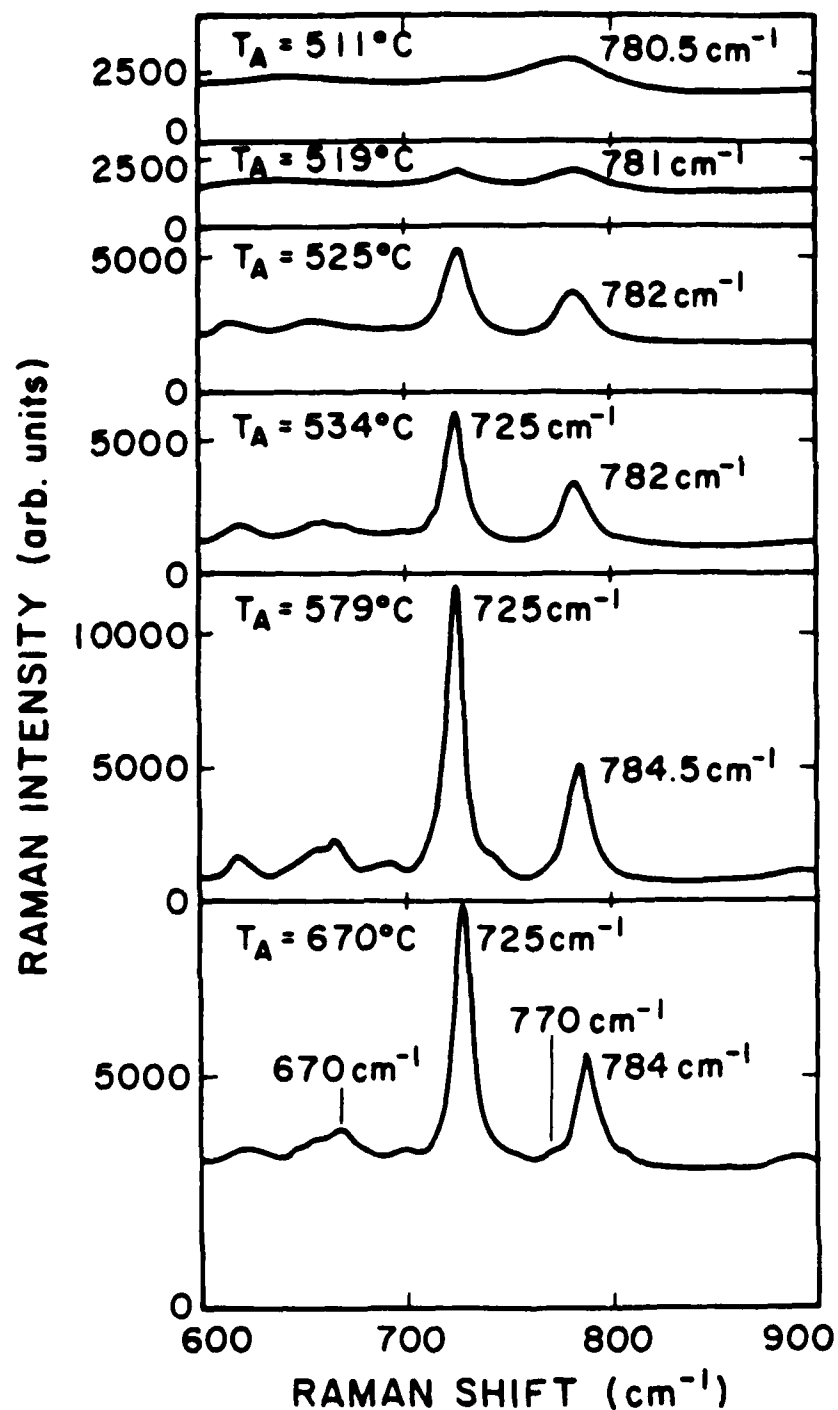


Figure 1f: Raman Spectra of $B_2O_3-0.5Li_2O-0.15Li_2SO_4$ for Different Annealing Temperatures Focussed at the Frequency Region of the Characteristic Modes for Crystalline Diborate. Spectra taken with a laser beam of 514.5-nm and power 250 mW. The instrumental resolution is 2 cm^{-1} .

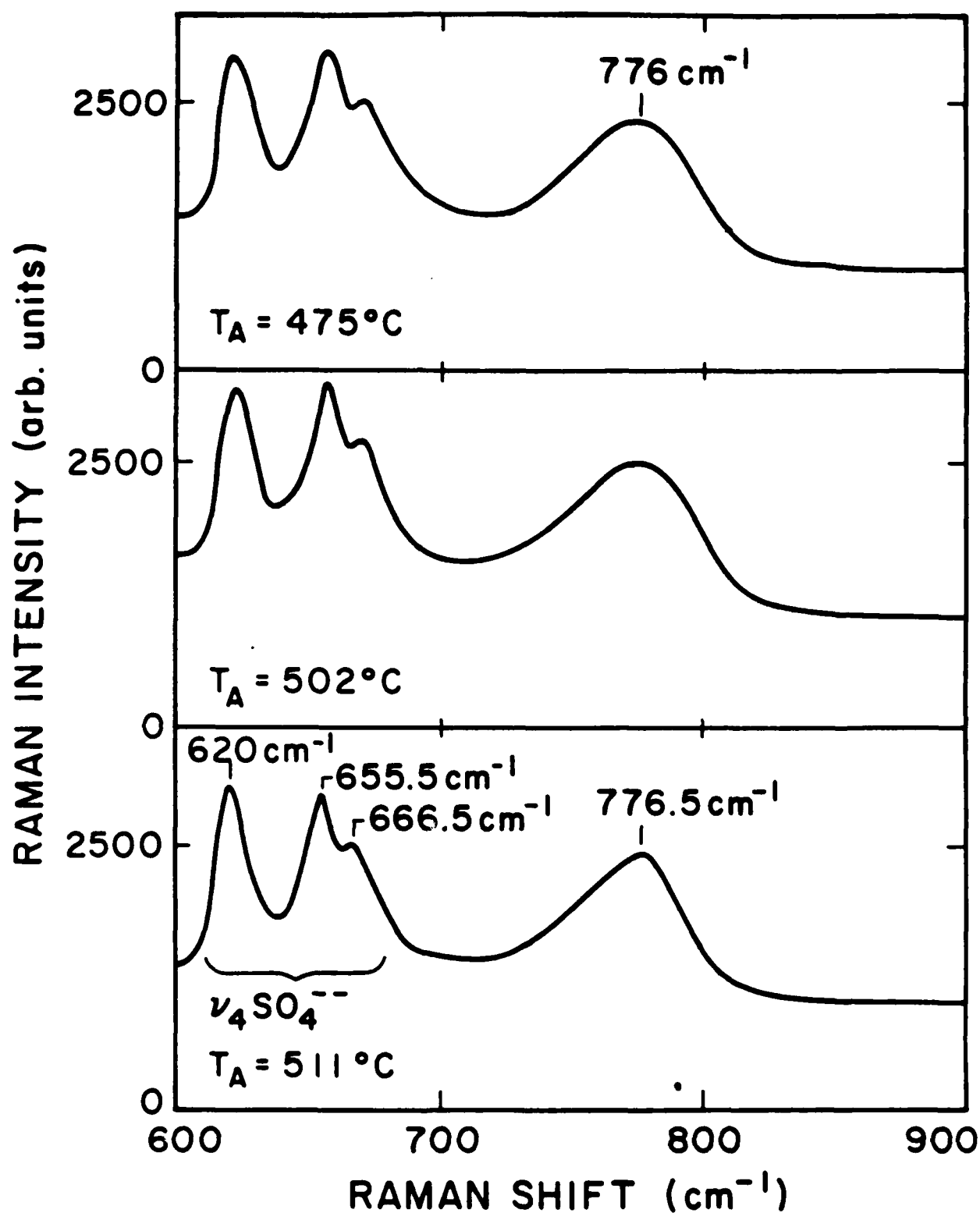


Figure 16: Raman Spectra of $\text{B}_2\text{O}_30.7\text{Li}_2\text{O}-0.42\text{Li}_2\text{SO}_4$ for Different Annealing Temperatures.

observed in the initial stage before the crystallization.

During the crystallization process, we expect that in the first stage the formation of diborate groups gives also BO_3 groups connected between them or between borate rings. Such groups contain non-bridging oxygens and consequently bind Li^+ ions with strong partial covalency. Here we find a possible explanation for the conductivity decrease observed before the lithium sulfate crystallization. Then, in the second stage, the lithium salt crystallizes and all the free Li^+ ions are trapped by the SO_4^{--} anions.

In the glassy state, where the ionic conductivity is high, the dopant Li_2SO_4 is ionized to give highly mobile Li^+ ions and immobile SO_4^{--} ions. The Li^+ ions lead to the high conductivity. This system is analogous to an aqueous solution of an electrolyte such as NaCl . We shall therefore apply Debye-Hückel theory to develop a physical understanding of the conductivity of $\text{B}_2\text{O}_3\text{-}0.5\text{Li}_2\text{O-xLi}_2\text{SO}_4$ as a function of composition x and temperature T . The concentration and mobility of free Li^+ ions will be calculated as a function of composition and temperature. Using these results the conductivity will be calculated.

1.6. Conclusion

This work suggests that the ionic conductivity of $\text{B}_2\text{O}_3\text{-}0.5\text{Li}_2\text{O-}0.1\text{Li}_2\text{SO}_4$ is modified by the structure of the matrix. The conductivity increases in the glassy state to reach $7 \times 10^{-6} \Omega^{-1} \text{cm}^{-1}$. Raman scattering shows the structural changes corresponding to the different stages of the conductivity

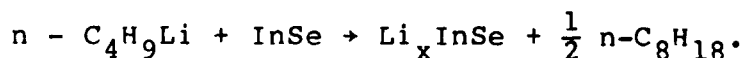
behavior. A mechanism which involves the appearance of non-bridging oxygen during the transformation of borate rings into diborate groups is proposed for describing the conductivity experiments.

II. Intercalation in Layered Compounds

1. Characteristics of the Intercalation Process

Lithium intercalation in InSe single crystals has been performed for the first time in the Laboratoire de Physique des Solides de l'Université Pierre et Marie Curie, Paris. The results obtained by E. Hatzikraniotis, C. Julien and M. Balkanski have been presented for the first time at the NATO-AST Conference in Portugal, 1984, on Solid State Batteries and published in Materials Research Bulletin 1984.

Chemical insertion of Li in InSe is obtained by immersion of a single crystal of InSe in a 1.6 M solution of n-butyllithium in hexane. Spontaneous intercalation is produced under these conditions according to the reaction



The reaction lasts for a long time under an inert atmosphere.

The following steps should be distinguished in this reaction.

- 1) Pre-equilibrium in the solution generating the active species: monomer, dimer and trimer of $n-C_4H_9Li$
- 2) Surface adsorption and activation of the absorbant ($n-C_4H_9Li$)
- 3) Electron transfer $e + Li$ bound to the solid
- 4) Diffusion of Li into the lattice

5) Ionization of Li

6) Dimerisation, diffusion of the alkane in the solution and production of octane.

The positions of the Li ions in the Van der Waals gaps of InSe are shown in Figure 17.

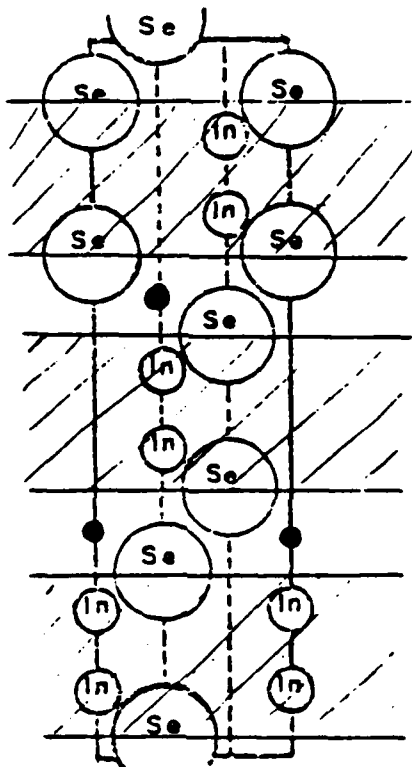


Figure 17. Positions of Li⁺ Ions (Solid Circles) in the Van der Waals Gap.

No indication of staging has been observed in this process of intercalation, but a saturation as a function of time has been observed. When lithium is intercalated into the layer compound InSe, electrical conductivity measurements indicate that the rate of intercalation is large at first, then decreases, and finally

approaches zero. This behavior indicates that there is a maximum or saturation value of the lithium concentration that can be achieved. A physical picture of this saturation behavior is as follows. The lithium atoms enter the Van der Waals gap between adjacent InSe layers. The 2S electrons of the lithium atoms ionize and transfer to a two-dimensional potential well in one of the adjacent InSe layers. As more lithium atoms are intercalated, the Fermi energy E_F of the electrons in the potential well rises as a consequence of the Fermi-Dirac statistics obeyed by the electrons. When the Fermi energy becomes equal to the energy of a 2S electron in a lithium atom, the transfer of electrons from the atoms to the potential well will cease and the electrical conductivity due to the electrons in the potential well will saturate. Calculations will be made of the corresponding value of the saturation concentration of lithium atoms using the experimental value of the lithium-atom ionization energy E_I and treating the potential well depth V_0 as an adjustable parameter. By fitting the experimental data, the value of the potential well depth will be determined. See Figure 18.

Following the completion of the above calculation, a more sophisticated calculation will be made using density functional theory and treating the Coulomb, exchange, and correlation interactions explicitly. The density profile of the electrons in the InSe layers will be determined as a function of lithium atom content, and the potential energy function for the motion of a lithium ion in the Van der Waals gap will be determined.

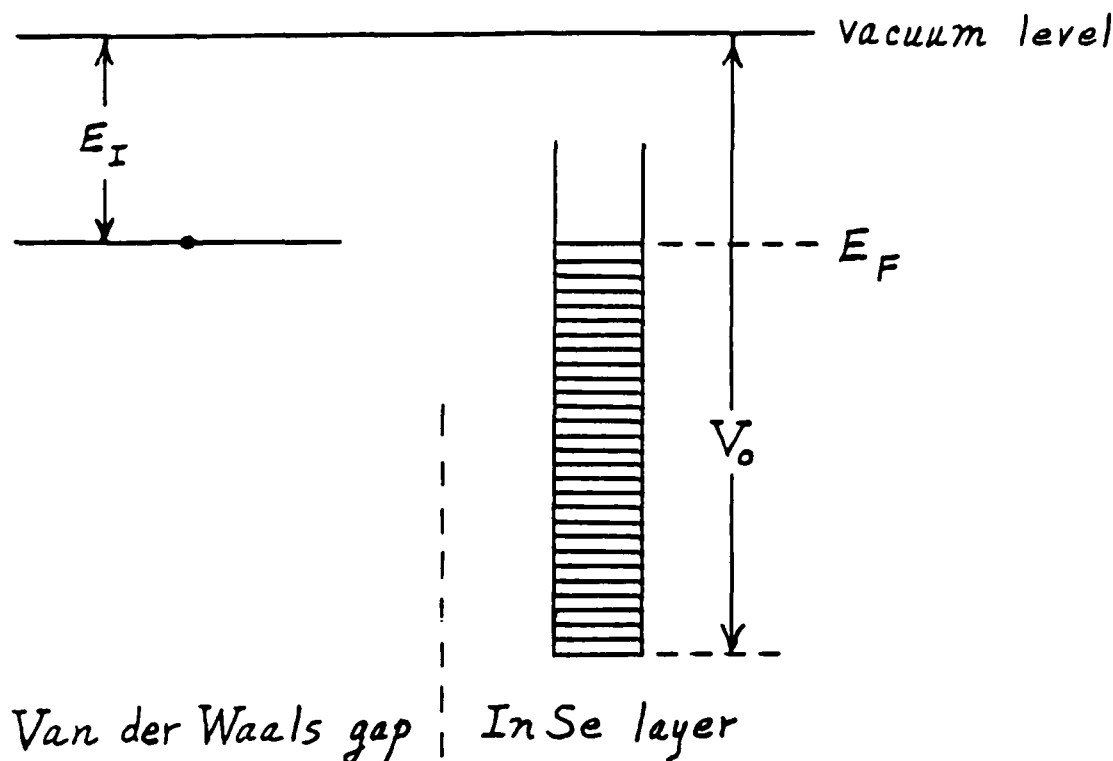


Figure 18. Energy Level Diagram for Intercalated Lithium Under Saturated Conditions

2. Intercalation

In the preceding section, a description was presented of the process whereby lithium atoms are intercalated into the layered compound indium selenide, InSe. As intercalation proceeds, the electrical resistivity of the InSe decreases, indicating that electrons are being ionized off of the Li atoms and entering the conduction band of the InSe. Eventually, the InSe can become saturated with lithium and its resistivity will cease decreasing. In the present report we analyze the experimental data for the time evolution of intercalation using a simple theoretical model.

2.1. Time Evolution of Intercalation

The intercalation of Li into InSe is achieved by immersing a single crystal of InSe into a 1.6 M solution of n-butyllithium in hexane. Experimental measurements of the resistivity of the InSe during intercalation have been made by C. Julien and coworkers in the laboratory of Professor M. Balkanski in Paris. The results for the resistivity as a function of time of intercalation are shown in Figure 19. The resistivity initially drops quite rapidly and then levels off. Saturation

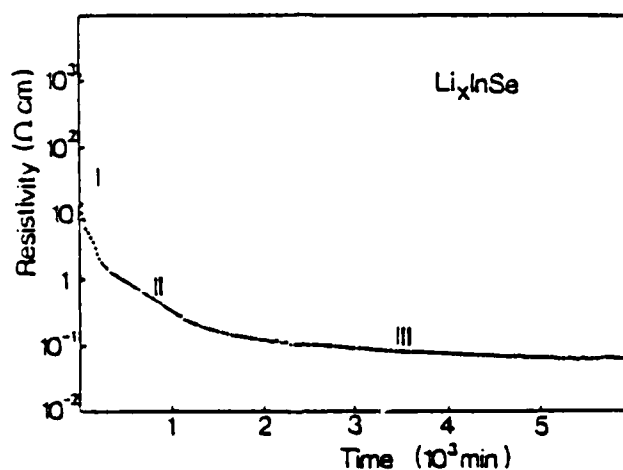


Fig. 19. Resistivity Versus Time Curve During Li-InSe Intercalation at Room Temperature

might be approached at the largest times. However, this does not seem to be the case. We must beware of the logarithmic scale used on the vertical axis in Figure 19. If we plot the reciprocal of the resistivity, or conductivity, versus time of intercalation, we obtain the plot shown in Figure 20. We see

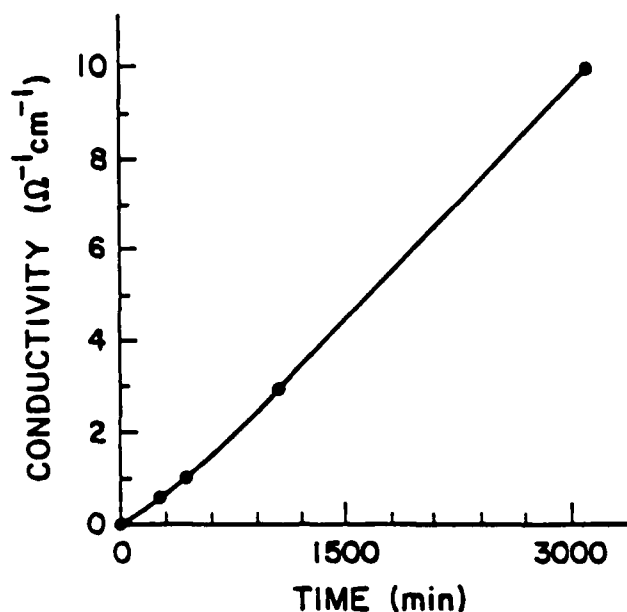


Figure 20. Conductivity Versus Time Curve During Li-InSe Intercalation at Room Temperature

that the conductivity is very nearly a linear function of time over the interval considered and that no evidence of saturation is evident. Viewed in this light, the experimental data are consistent with the picture that the conduction electron concentration in the InSe is increasing linearly with time as a consequence of a corresponding linear increase in Li concentration with time.

2.2. Analysis of Saturation of Electrical Conductivity During Intercalation

Although saturation of the conductivity has not yet been achieved experimentally, it should be attainable after

sufficiently long periods of intercalation. In our physical picture, the intercalated Li atoms enter the Van der Waals gap between adjacent InSe layers and lose their 2S electrons to one or the other of the two-dimensional potential wells in the adjacent InSe layers. As more Li atoms are intercalated, the Fermi energy E_F of the electrons in the potential well, rises as a consequence of the Fermi-Dirac statistics obeyed by the electrons. When the Fermi energy becomes equal to the energy of a 2S electron in a lithium atom, the transfer of electrons from the atoms to the potential well will cease and the electrical conductivity due to the electrons in the potential well will saturate. The energy level situation at saturation is shown in Figure 18. Clearly, the greater the depth of the potential well V_0 , the greater the fraction of electrons transferred from the Li atoms to the potential well.

We have carried out a Thomas-Fermi analysis of the fraction of electrons transferred as a function of the well depth. Let the width of the Van der Waals gap be a_0 and the periodicity length perpendicular to the planes of the InSe be c_0 . The quantity $c_0 - a_0$ is therefore the width of the potential well. Within the well, the potential has the constant value V_0 . The Li^+ ions are assumed to be uniformly distributed over two planes symmetrically disposed about the middle of the Van der Waals gap and a distance C_+ apart.

The Thomas-Fermi procedure utilizes an energy functional of the electron number density which consists of the kinetic energy and electrostatic potential energy. By minimizing the energy

functional with respect to variations in number density, one obtains a relation between the latter and the electric potential. Combining this relation with Poisson's equation and applying the appropriate boundary conditions leads to an expression for the number density as a function of position in the system. The fraction of the electrons located within the InSe potential well can then be readily calculated.

To set up the energy functional, we introduce the number density of the electrons n and of the Li^+ ions ρ and the electrostatic potential of the electrons V_1 and of the Li^+ ions V_2 . We regard the potential well associated with an InSe layer as arising from an external charge distribution ρ_{ext} and external potential V_{ext} which satisfies

$$\begin{aligned} V_{\text{ext}}(z) &= V_0, & \frac{a_0}{2} < z < \frac{c_0}{2} & \quad (\text{InSe}) \\ &= 0, & 0 < z < \frac{a_0}{2} & \quad (\text{Van der Waals gap}) \end{aligned}$$

with $V_{\text{ext}}(z)$ in other regions given by symmetry and periodicity. The charges are assumed to form continuous charge distributions varying only in the z -direction normal to the InSe layers. The energy functional can be written as

$$\begin{aligned} E[n] &= \frac{e}{2} \int [V_1(z) - V_2(z) - V_{\text{ext}}(z)][n(z) - \rho(z) - \rho_{\text{ext}}(z)]dz \\ &+ \int \epsilon_b(n(z))n(z)dz \end{aligned} \quad (1)$$

corresponds to their kinetic energy in the InSe layer. We assume that the electrons can be approximated by a two-dimensional system for which $\epsilon_b(n(z))$ is given by

$$\epsilon_b(n(z)) = \frac{1}{2} \beta n(z) \quad (2)$$

where $\beta = \pi^2 \hbar^2 c_0 / m^*$ and m^* is the electron effective mass. If Equation 2 is substituted into Equation 1 and the energy functional is then minimized with respect to variations in $n(z)$, one obtains the following equation relating $n(z)$ to the potentials:

$$\frac{e}{2} [V_2(z) - V_1(z) + V_{\text{ext}}(z)] = \beta n(z) \quad (3)$$

It proves to be convenient to introduce atomic units where energy is measured in units of the Rydberg, $me^4/2\hbar^2$, and length is measured in units of the Bohr radius, $\hbar^2/me^2 \equiv a_B$. Equation 3 can then be written as

$$\bar{n}(\xi) = \frac{m^* a_B}{4\pi m c_0} \phi(\xi) \quad (4)$$

where $\xi = z/a_B$, $\bar{n} = a_B^3 n$, and

$$\phi(\xi) = \left(\frac{2\hbar^2}{me^3} \right) [V_2(a_B \xi) - V_1(a_B \xi) + V_{\text{ext}}(a_B \xi)] \quad (5)$$

The second equation relating \bar{n} and ϕ that we need is

Poisson's equation. It is given by

$$\frac{d^2 \phi(\xi)}{d\xi^2} = \frac{8\pi}{\epsilon(\xi)} [\bar{n}(\xi) - \bar{\rho}(\xi) - \bar{\rho}_{\text{ext}}(\xi)] \quad (6)$$

where $\bar{\rho}(\xi)$ is the number density of the lithium ions, $\bar{\rho}_{\text{ext}}(\xi)$ is the number density of the charges that give rise to the external potential V_{ext} , and $\epsilon(\xi)$ is the dielectric constant. The relationship between $\bar{\rho}_{\text{ext}}$ and V_{ext} is given by the Poisson equation

$$\frac{d^2 V_{\text{ext}}}{d\xi^2} = - \frac{4\pi e}{\epsilon(\xi) a_B} \bar{\rho}_{\text{ext}}(\xi) \quad .$$

If we eliminate $\bar{n}(\xi)$ from Equation 6 using Equation 4, we obtain the equation for $\phi(\xi)$ in the form

$$\frac{d^2 \phi(\xi)}{d\xi^2} = \frac{2\mu(\xi)}{c\epsilon(\xi)} \phi(\xi) - \frac{8\pi}{\epsilon(\xi)} [\bar{\rho}(\xi) + \bar{\rho}_{\text{ext}}(\xi)] \quad (7)$$

where $c = c_0/a_B$ and $\mu(\xi) = m^*(\xi)/m$. In order to solve the equation, we introduce an approximation. The Li^+ ions are assumed to lie on two-dimensional sheets located at the boundaries between the Van der Waals gaps and the InSe layers. In the range $0 < \xi < c/2$,

$$\bar{\rho}(\xi) = \bar{\sigma} \delta\left(\xi - \frac{\alpha_0}{2}\right) \quad (8)$$

where $\bar{\sigma}$ is the charge density of the Li^+ ions in the sheet and $\alpha_0 = a_0/a_B$. The charge sheet leads to a discontinuity of the

derivative of the potential at $\xi = \alpha_0/2$ given by

$$\phi'(\xi \rightarrow \frac{\alpha_0}{2}^+) - \phi'(\xi \rightarrow \frac{\alpha_0}{2}^-) = -p_0 \quad (9)$$

where $p_0 = 8\pi\bar{\sigma}/\bar{\epsilon}$ and $\bar{\epsilon}$ is the mean dielectric constant. The charge density $\bar{\rho}_{\text{ext}}(\xi)$ corresponds to an electric dipole layer at $\xi = \alpha_0/2$ that produces the potential well and leads to the discontinuity of the potential $\phi(\xi)$

$$\phi(\xi \rightarrow \frac{\alpha_0}{2}^+) - \phi(\xi \rightarrow \frac{\alpha_0}{2}^-) = v_0 \quad (10)$$

From the above consideration we can find $\phi(\xi)$ by solving the differential equation

$$\frac{d^2\phi}{d\xi^2} = \tau_i^2 \phi, \quad \tau_i^2 = \frac{2\mu_i}{C\epsilon_i}, \quad i = 1, 2, \quad (11)$$

subject to the boundary conditions given by Equations 9 and 10 and the boundary conditions imposed by the periodicity of the system given by

$$\phi'(\xi = 0) = 0 \quad (12a)$$

$$\phi'(\xi = \frac{C}{2}) = 0 \quad (12b)$$

The values of $i = 1, 2$ refer to the regions $0 < \xi < \frac{\alpha_0}{2}$ and $\frac{\alpha_0}{2} < \xi < \frac{C}{2}$, respectively. The solution is found to be

$$\phi(\xi) = A_1 \cosh \xi \tau_1, \quad 0 < \xi < \frac{\alpha_0}{2} \quad (13a)$$

$$= A_2 \cosh \left[\left(\xi - \frac{c}{2} \right) \tau_2 \right], \quad \frac{\alpha_0}{2} < \xi < \frac{c}{2} \quad (13b)$$

where

$$A_1 = \frac{p_0 \cosh \left(\frac{c-\alpha_0}{2} \tau_2 - V_0 \sinh \left(\frac{c-\alpha_0}{2} \tau_2 \right)}{\sinh \left(\frac{c}{2} \tau_2 + \frac{\alpha_0}{2} (\tau_1 - \tau_2) \right)} \quad (14a)$$

$$A_2 = \frac{p_0 \cosh \frac{\alpha_0}{2} \tau_1 + V_0 \sinh \frac{\alpha_0}{2} \tau_1}{\sinh \left(\frac{c}{2} \tau_2 + \frac{\alpha_0}{2} (\tau_1 - \tau_2) \right)} \quad (14b)$$

The electron density $\bar{n}(\xi)$ can be calculated from $\phi(\xi)$ using Equation 4. The electron charge in the Van der Waals gap, Q_1 , and in the InSe layer, Q_2 , can then be calculated and are found to be

$$\begin{aligned} Q_1 &= -2e \int_0^{\alpha_0/2} d\xi \bar{n}(\xi) \\ &= \frac{-e\epsilon_1 \tau_1}{4\pi} \frac{p_0 \cosh \frac{c-\alpha_0}{2} \tau_2 - V_0 \sinh \frac{c-\alpha_0}{2} \tau_2}{\sinh \left(\frac{c}{2} \tau_2 + \frac{\alpha_0}{2} (\tau_1 - \tau_2) \right)} \sinh \frac{\alpha_0}{2} \tau_1 \quad (15a) \end{aligned}$$

$$\begin{aligned} Q_2 &= -2e \int_{\alpha_0/2}^{c/2} d\xi \bar{n}(\xi) \\ &= \frac{-e\epsilon_2 \tau_2}{4\pi} \frac{p_0 \cosh \frac{\alpha_0}{2} \tau_1 + V_0 \sinh \frac{\alpha_0}{2} \tau_1}{\sinh \left(\frac{c}{2} \tau_2 + \frac{\alpha_0}{2} (\tau_1 - \tau_2) \right)} \sinh \frac{c-\alpha_0}{2} \tau_2 \quad (15b) \end{aligned}$$

The fraction of the electron charge that is transferred to the InSe layer is given by

$$f = \frac{Q_2}{Q_1 + Q_2}$$

$$= \left(\cosh \frac{\alpha_0}{2} \bar{\tau} + \frac{V_0}{p_0} \sinh \frac{\alpha_0}{2} \bar{\tau} \right) \frac{\sinh \frac{c - \alpha_0}{2} \bar{\tau}}{\sinh \frac{c}{2} \bar{\tau}} \quad (16)$$

where for simplicity we have replaced the τ_i and the ϵ_i by their average values $\bar{\tau}$ and $\bar{\epsilon}$, respectively.

The fraction f increases with increasing potential well depth V_0 until a critical value of V_0 is reached for which $f = 1$ and all of the electrons have been transferred from the lithium atoms to the InSe layer. In Figure 21 is given a plot of f versus V_0/p_0 . We see that f increases linearly with V_0 . The critical value of V_0 is found to be $V_{\text{crit}} = 1.043 p_0$. The

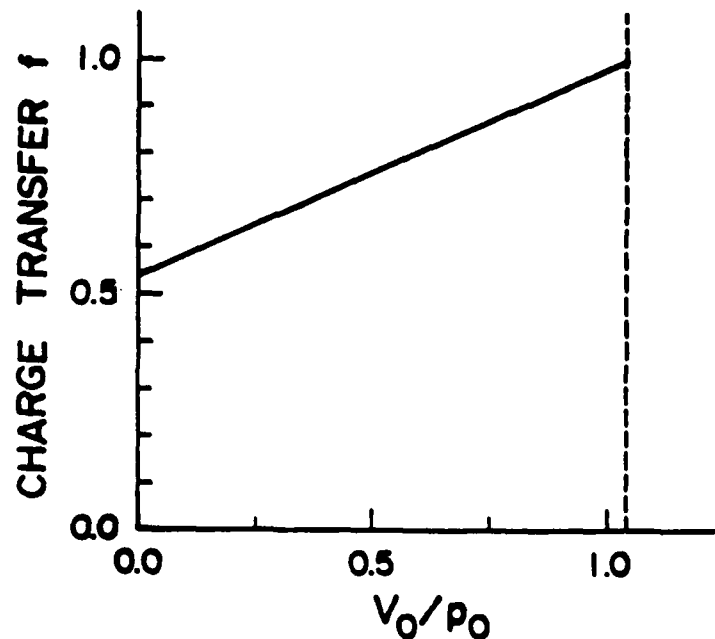


Figure 21. Charge Transfer at Saturation Versus Potential Well Depth for Li-InSe Intercalation

minimum value of f is not zero because the Li^+ ions are assumed to be at the interface between the Van der Waals gap and the InSe layer. A more realistic calculation is currently underway in which the Li^+ ions are moved into the Van der Waals gap away from the interface.

3. Photoluminescence in Layered InSe

The layered III-VI compounds function as positive electrodes in lithium batteries. In this study we have prepared InSe to observe its optical properties and the effects on the electronic structure of chemical lithium intercalation.

Optical properties have been mainly investigated by photoluminescence (PL) and Raman spectroscopy (RS). The effects of Li intercalation on the emission spectrum and on the phonon scattering spectrum are presented and an interpretation of the observations is given.

Lithium intercalation of InSe was performed by direct reaction with *n*-butyl lithium in 1.6 M solution dissolved in hexane. Experiments were carried out in a controlled atmosphere and electrical properties were monitored during intercalation. Optical measurements were done after more than four weeks relaxation time.

InSe is an *n*-type semiconductor with an electronic band structure almost flat for any direction within the layer plane. The absorption spectrum consists of edges with excitonic absorption peaks at each step between different valence bands and the conduction band, such as other layered compounds or super lattice semiconductors. Consequently, we have studied PL spectra

associated with the two first edges in the absorption coefficient near 1.35 eV and 2.60 eV.

The direct gap at 1.325 eV and the indirect one at 1.300 eV are very close. In the PL spectrum at 5K of the pure InSe, four groups of lines are associated with these transitions (Figure 22a): (1) the narrow excitonic line at 1.338 eV in coincidence with the free exciton; (2) the bound excitonic lines at 1.334 eV and 1.331 eV, with thermal dissociation energies which correspond to the energy separations between the free exciton and these peaks (the time-resolved PL measurements confirm these assignments); (3) a broad band with three peaks at 1.322 eV, 1.317 eV and 1.311 eV. This band appears with a 10 ns delay time

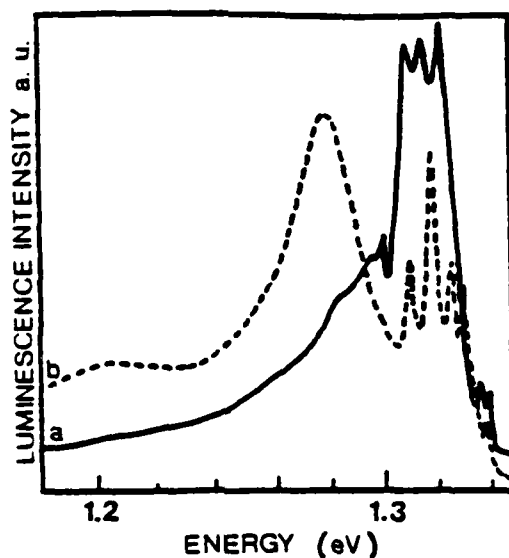


Figure 22. Photoluminescence Spectra of InSe Before (a) and After Lithium Intercalation (b) at 5 K Under 1.916 eV Excitation of a Kr⁺ Laser.

and shifts to lower energy with increasing time delay. This band seems to be due to radiative recombination of the electron-hole pairs in electron-hole liquid (EHL) or of the donor-acceptor pair (DAP); (4) small bands at lower energy than the indirect band a broad band at 2.545 eV due to the radiative recombination of the exciton.

After intercalation with lithium, PL at 5K is given in Figure 22b and we can see that the first two excitonic lines remain with a small shift at low energy of 3 meV and a similar shift appears at 2.545 eV. The EHL or DAP peaks are better resolved and are shifted to higher energy. Two new dominant bands appear at 1.278 eV and 1.206 eV. The maximum energy of these bands increases with temperature and this behavior is

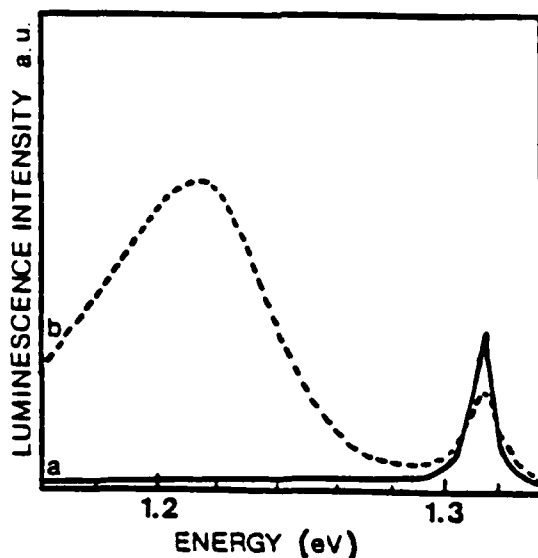


Figure 23. Photoluminescence Spectra of InSe Before (a) and After Lithium Intercalation (b) at 100 K Under 1.916 eV Excitation of a Kr⁺ Laser.

opposite to those of the other lines. The decreasing intensities of these two bands with increasing temperature are similar to those of the bound excitons with higher thermal dissociation energies.

At higher temperatures, the 1.278 eV band disappears with the bound excitonic peaks and the EHL or DAP band. At 100 K, as shown in Figure 23, we have only two bands: the radiative free exciton band and the 1.214 eV broad band. The 1.278 eV line can be attributed to the phonon assisted recombination of an indirect exciton bound to the Li-donor and the 1.206 eV broad band to phonon assisted donor-acceptor pair recombinations.

In the RS spectra, the ratio between the three-dimensional LO phonon and the two-dimensional one increases when lithium is incorporated. Two new small peaks at 132 cm⁻¹ and 190 cm⁻¹ appear near the A₁'-mode (118 cm⁻¹) and the A₂"-mode (182 cm⁻¹) respectively. The origin of these phenomena seems to be due to the change of dimensionality in the crystal related to the binding between the Li atoms and the layers in the crystal. This increasing binding is probably responsible for the small shift of the free excitonic line in the InSe:Li PL spectra.

END

2-87

DTIC